Impact of ENSO on the Atmospheric Variability over the North Atlantic in Late Winter—Role of Transient Eddies

YING LI

Program in Atmospheric and Oceanic Sciences, Princeton University, Princeton, New Jersey

NGAR-CHEUNG LAU

NOAA/Geophysical Fluid Dynamics Laboratory, Princeton, New Jersey

ABSTRACT

The dynamical mechanism for the late-winter teleconnection between El Niño–Southern Oscillation (ENSO) and the North Atlantic Oscillation (NAO) is examined using the output from a 2000-yr integration of a coupled general circulation model (GCM). The coupled model captures many salient features of the observed behavior of both ENSO and NAO, as well as their impact on the surface climate in late winter. Both the observational and model data indicate more occurrences of negative phase of NAO in late winter during El Niño events, and positive NAO in La Niña episodes.

The potential role of high-frequency transient eddies in the above teleconnection is diagnosed. During El Niño winters, the intensified transient disturbances along the equatorward-shifted North Pacific storm track extend their influences farther downstream. The eddy-induced negative height tendencies are found to be more coherent and stronger over North Atlantic than that over North Pacific. These negative height tendencies over the North Atlantic are coincident with the southern lobe of NAO, and thus favor more occurrences of negative NAO events.

During those El Niño winters with relatively strong SST warming in eastern equatorial Pacific, the eastward extension of eddy activity is reinforced by the enhanced near-surface baroclinicity over the subtropical eastern Pacific. This flow environment supports a stronger linkage between the Pacific and Atlantic storm tracks, and is more conducive to a negative NAO phase.

These model results are supported by a parallel analysis of various observational datasets. It is further demonstrated that these transient eddy effects can be reproduced in atmospheric GCM integrations subjected to ENSO-related SST forcing in the tropical Pacific.

1. Introduction

El Niño–Southern Oscillation (ENSO), as the dominant pattern of interannual climate variability, has strong influences on the atmospheric circulation around the globe (e.g., Bjerknes 1969; Horel and Wallace 1981; Trenberth et al. 1998). Particular attention has been devoted to the relationships between ENSO and various meteorological anomalies associated with the Pacific–North American (PNA) teleconnection pattern (Wallace and Gutzler 1981). However, some studies have pointed out that the ENSO-related circulation pattern is distinct

from the internally generated PNA pattern (e.g., Straus and Shukla 2002; Nigam 2003).

North Atlantic Oscillation (NAO) is another prominent mode of interannual variability in the Northern Hemisphere extratropics (Branston and Livezey 1987; Hurrell 1995a; Hurrell and van Loon 1997). It is characterized by opposing changes in the sea level pressure (SLP) centers near the Azores in the subtropical North Atlantic (NA) and Iceland. Fluctuations in amplitude and polarity of the NAO exert a strong influence on the climate of the NA basin and the surrounding land areas (e.g., Walker and Bliss 1932; van Loon and Rogers 1978; Thompson and Wallace 2001).

While the responses of the climate over the North Pacific (NP) and North America to ENSO are well known (see Trenberth et al. 1998 for a review), the effects of ENSO on the North Atlantic–European region are less

Corresponding author address: Ying Li, Program in Atmospheric and Oceanic Sciences, Princeton University, 201 Forrestal Road, Princeton, NJ 08544.
E-mail: yingl@princeton.edu

certain (Greatbatch et al. 2004; Toniazzo and Scaife 2006; Brönnimann 2007). It was indicated in some earlier studies that the association between ENSO and NAO is weak and difficult to detect in short observational records (Rogers 1984; Fraedrich 1994). More recent works based on observational data (Fraedrich and Müller 1992; Dong et al. 2000; Moron and Gouirand 2003; Pozo-Vázquez et al. 2001, 2005; Brönnimann et al. 2004, 2007) and numerical experimentation (Merkel and Latif 2002; Gouirand et al. 2007; Ineson and Scaife 2009) indicate that ENSO can extend its influence to the remote North Atlantic–European sector, with responses in early winter being different from those in late winter. Some authors note a nonstationary ENSO response over Europe (Greatbatch et al. 2004), whereas Brönnimann et al. (2007) find a consistent and stationary relationship between ENSO and the late-winter climate in Europe using reconstructed SLP data for the past 300 years. Nonlinearity in the response of SLP over the NA to the strength of El Niño (Toniazzo and Scaife 2006; Bell et al. 2009) and to the polarity of ENSO phase (Pozo-Vázquez et al. 2001, 2005; Gouirand and Moron 2003) have also been noted. Despite the considerable level of interevent variability (e.g., Hamilton 1988; Gouirand and Moron 2003; Mathieu et al. 2004; Larkin and Harrison 2005; Gouirand et al. 2007), a majority of observational and modeling studies shows that the following features are prevalent in the late winters of El Niño events: high SLP anomaly from Iceland to Scandinavia, low SLP anomaly from the east coast of the United States to the Black Sea, as well as cold and dry conditions over northern Europe, and warm and wet conditions over parts of the Mediterranean (Fraedrich and Müller 1992; Fraedrich 1994; Merkel and Latif 2002; Moron and Gouirand 2003; Gouirand et al. 2007). A possible link between the North Atlantic–European climate and ENSO has important implications for seasonal forecasts in that region.

An equatorward shift and eastward extension of the Pacific storm track during El Niño have been noted in previous studies (e.g., Hoerling and Ting 1994; Straus and Shukla 1997; Held et al. 1989; Chang 1998; Zhang and Held 1999; Seager et al. 2003; Lau et al. 2005; Orlanski 2005). Changes in the midlatitude storm tracks during El Niño events alter the vorticity flux by transient synoptic eddies, thereby modulating the amplitude and structure of the extratropical wave trains initiated by tropical sea surface temperature (SST) anomalies (Kok and Opsteegh 1985; Held et al. 1989; Hoerling and Ting 1994; Kushnir et al. 2002; Orlanski 2005, among others). To our knowledge, the prior studies have not devoted much attention to the effects of transient eddies on the flow pattern downstream of the PNA sector. A few other studies has pointed out that anticyclonic and cyclonic breaking of the synoptic eddies could lead to the formation of the positive and negative phase of the NAO, respectively (e.g., Benedict et al. 2004; Franzke et al. 2004; Rivière and Orlanski 2007). In particular, Rivière and Orlanski (2007) noted that waves originating from the eastern Pacific and breaking cyclonically or anticyclonically over the Atlantic are crucial for determining the NAO phase. This upstream influence from the eastern Pacific suggests a role for the transient eddies in linking between flow patterns over the NP and NA. Given the importance of the positive feedback between high-frequency eddies and the quasi-stationary flow in maintaining the NAO (Lau 1988; Branstator 1992; Hurrell 1995b; Nakamura et al. 1997), it is important to extend the scope of the previous studies by investigating the nature of transient eddy forcing in the North Atlantic–European region during ENSO events.

The purpose of the present work is to study the effect of ENSO on the behavior of transient eddies in both the Pacific and Atlantic sectors, and to evaluate the impact of the accompanying eddy forcings on the phase of NAO. While this work improves our understanding of ENSO forcing of eddy–mean flow interaction in both the NP and NA sectors, it does not directly address issues pertaining to causes and effects. In a follow-up article (Li and Lau 2011, manuscript submitted to *J. Climate*), we will provide additional evidence in support of ENSO impact on the downstream development of the wave packets from the Pacific toward the eastern Atlantic, and subsequent feedback onto the mean flow. The primary database for this work is the output from a 2000-yr integration of a coupled general circulation model (GCM). In view of the large variability of the atmospheric responses in the remote North Atlantic–European sector during individual ENSO events (Hamilton 1988; Kumar and Hoerling 1997; Toniazzo and Scaife 2006), it is difficult to identify statistically significant signals on the basis of limited observational records. The advantage of utilizing an extended GCM integration in this study is that the output from this experiment allows for adequate sampling of various features of interest, so that their mutual relationships can be established with a higher degree of confidence. Focusing on a model run with preindustrial climate forcing allows us to study the natural model variability. Ultimately, the analysis can be applied to the understanding and assessment of future climate change in light of the results by Müller and Roeckner (2006), who predict a strengthened negative correlation between ENSO and the NAO indices in the future.

The GCM as well as the observational datasets used for validating the model results are described in section 2. Simulated and observed aspects of the impacts of ENSO and the NAO on the atmospheric variability in

the NA sector are presented, and the significant linkage between the two modes is documented in section 3. The characteristics of the simulated and observed synoptic eddies, their interaction with the monthly mean flow, and the vorticity forcing in terms of eddy-induced geopotential height tendencies are shown and discussed in section 4 for the warm and cold phases of the ENSO anomalies. In section 5, ensemble atmospheric GCM (AGCM) integrations, with anomalous SST prescribed only in the tropical Pacific, are designed and tested for their ability to reproduce some of the results described in section 4. The flow patterns and SST environment associated with various combinations of ENSO and NAO phases are examined in section 6. Summary and discussion are given in section 7.

2. Data and methodology

a. Model description

The model data analyzed in this study is generated by a 2000-yr-long integration of the Geophysical Fluid Dynamics Laboratory (GFDL) Climate Model version 2.1 (CM2.1; Delworth et al. 2006; Wittenberg 2009), with radiative forcing being fixed at the preindustrial (1860) level throughout the experiment. The resolution of the atmospheric component of CM2.1 (hereafter referred to as AM2.1) is 2° latitude × 2.5° longitude. The 24 vertical levels are structured in a hybrid coordinate, with 5 levels in the stratosphere and a model top at about 3 mb. The physics packages employed in AM2.1 are described by the GFDL Global Atmospheric Model Development Team (2004). The dynamical core of this model uses the finite-volume method coded by Lin (2004). The oceanic component of CM2.1 builds on the fourth generation of the Modular Ocean Model (MOM4), as described in Griffies et al. (2004). The resolution is 1° latitude × 1° longitude, with meridional grid spacing decreasing to ⅓° toward the equator. There are altogether 50 vertical levels, with 22 levels being located in the top 220 m (Gnanadesikan et al. 2006). The atmosphere, ocean, land, and sea ice exchange fluxes once every 2 h, and fluxes are conserved within machine precision. The model has been run without any flux adjustments for over 2000 yr and exhibits no appreciable climate drifts in the quantities examined in this paper.

b. Observational datasets

The observational data used to compare with model findings include the following:

- Monthly precipitation data from the Global Precipitation Climatology Project (GPCP) version 2 (Adler et al. 2003). This is a product that merges satellite

microwave and infrared data with rain gauge observations and covers the 1979–2009 period.
- Surface air temperature (SAT), SLP, geopotential height, and upper-level wind (1948–present) from the National Centers for Environmental Prediction–National Center for Atmospheric Research (NCEP–NCAR) reanalysis (Kalnay et al. 1996).
- A recently released atmospheric reanalysis for the 1891–2008 period, hereafter referred to as the twentieth-century (20thC) dataset (Compo et al. 2006). This dataset is based primarily on the assimilation of surface pressure observations before the radiosonde era, and has been demonstrated to yield an adequate depiction of the large-scale tropospheric circulation features (Whitaker et al. 2004; Compo et al. 2006).
- Monthly mean SST from the National Oceanic and Atmospheric Administration (NOAA) extended reconstructed SST version 3 dataset (ERSST v3; see Smith et al. 2008; Xue et al. 2003).

c. Analysis tools

Storm-track characteristics are depicted using eddy variance and covariance statistics. Following Lau (1988), a 2–10-day bandpass Lanczos filter (Duchon 1979) with 41 weights is applied to the daily 500-mb geopotential height data Z at each grid point, and then the root-mean-square (rms) of the filtered height $(\overline{Z'^2})^{1/2}$ is computed. Here the prime represents the bandpass-filtered quantities and the overbar denotes time averaging over an individual winter month.

Extended Eliassen–Palm vectors (hereafter referred to as **E**) are used to illustrate the properties of transient eddies and local interactions between transient eddies and the time-mean flow (Hoskins et al. 1983). The horizontal components of **E** used in this study are given by Trenberth (1986):

$$\frac{1}{2}(\overline{v'^2} - \overline{u'^2})\mathbf{i} - \overline{u'v'}\mathbf{j}.$$

Here u, v are the zonal and meridional wind components, respectively. The **E** vectors point approximately in the direction of the wave energy propagation relative to the local time-mean flow. The divergence and curl of **E** indicate eddy-induced acceleration of the local mean zonal and meridional wind, respectively.

The barotropic feedback of the transient eddies on the quasi-stationary flow is illustrated by the eddy-induced geopotential height tendency associated with horizontal convergence of eddy vorticity flux at the 250-mb level as given by Lau and Holopainen (1984):

$$\left(\frac{\partial Z_{250}}{\partial t}\right)_{\text{eddy}} = \frac{f}{g}\nabla^{-2}[-\nabla \cdot (\overline{V'\zeta'})]. \qquad (1)$$
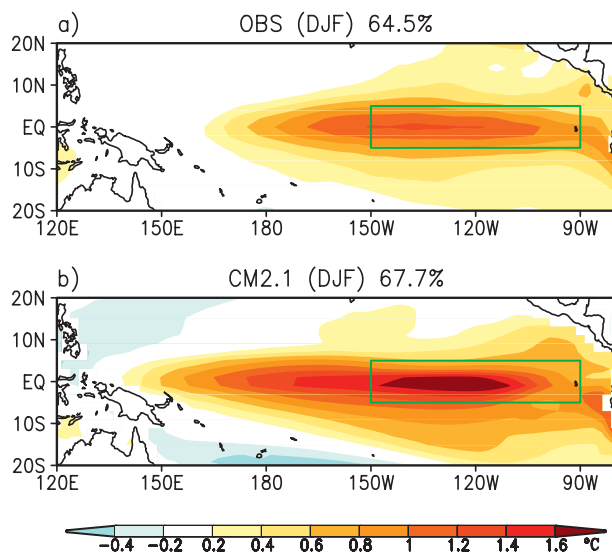
FIG. 1. Spatial patterns of the leading EOF of DJF-mean SST anomalies over the tropical Pacific based on the (a) NOAA ERSST V3 dataset for the 1948–2010 period and (b) CM2.1 simulation. The patterns show the regression coefficients of DJF-mean SST vs the standardized temporal coefficients of the EOF. Units: °C. These observed and simulated EOF modes account for 64.5% and 67.7% of the total variance, respectively. The rectangular outline depicts the Niño-3 region (5°S–5°N, 150°–90°W). The observed and simulated standard deviations of Niño-3 SST are 0.97° and 1.22°C, respectively.

Here Z_{250} is the geopotential height at 250 mb, **V** is the horizontal wind vector, ζ is the relative vorticity, f is the Coriolis parameter, and g is the acceleration due to gravity.

3. Simulation of ENSO and NAO variability

a. ENSO variability and its impacts on SLP over the North Pacific and North Atlantic

An empirical orthogonal function (EOF) analysis of December–February (DJF) mean SSTs over the tropical Pacific region is performed. The observed and simulated spatial patterns resulting from this EOF analysis are presented in Fig. 1. The observed (Fig. 1a) and simulated (Fig. 1b) patterns explain 64.5% and 67.7% of the total variance, respectively. The data value shown in these panels depict the local amplitudes of SST anomalies corresponding to one standard deviation of the temporal coefficients of the EOF. It is evident that the amplitude of SST variations in the model is higher than that in the observations, and the simulated SST anomaly extends too far westward to the equatorial western Pacific. We shall henceforth present the results based on the Niño-3 index (SST anomalies averaged over 5°S–5°N, 150°–90°W; see boxed area in Fig. 1). Analyses based on alternative

TABLE 1. List of observed El Niño and La Niña events selected using the DJF-mean Niño-3 index. The year of initiation of the selected ENSO event is designated as year(0); the following year is referred as year(1). The listed year corresponds to year(1). Years used for the composites in the NCEP–NCAR reanalysis dataset are in italics.

El Niño events									
1897	1900	1903	1912	1919	1926	1931	1941	*1958*	*1966*
1973	1977	*1983*	*1987*	*1992*	1995	*1998*	2003	2007	2010*
La Niña events									
1893	1894	1909	1910	1911	1917	1918	1923	1925	1934
1943	*1950*	*1956*	*1968*	*1971*	*1974*	*1976*	*1989*	*2000*	*2008*

* Recent El Niño event not covered by the 20thC reanalysis dataset.

indices [such as Niño-3.4 (5°S–5°N, 170°–120°W) and the temporal coefficients of the leading EOF of SST field] yield similar results.

A warm (cold) ENSO event is identified when the DJF-mean Niño-3 index is more than one standard deviation above (below) the time mean. This criterion yields 10 warm and 9 cold events based on the NOAA ERSST V3 dataset for the 1948–2010 period, and 19 warm and 20 cold events based on the same dataset for the 1891–2008 period. Table 1 lists the selected cases. Analogous analysis of the CM2.1 data yields 252 warm events and 215 cold events.

To investigate the phase locking of ENSO variability with the seasonal cycle, Fig. 2 shows the composite month-to-month evolution of the Niño-3 SST anomalies during El Niño and La Niña events for both observations and the CM2.1 simulation. For El Niño events, the observed anomaly peaks near December(0), while the corresponding model result shows large positive anomalies over a broad period, with a primary peak in February(1) that corresponds to the mature phase, and a secondary peak in August(0) resulting from the semiannual phase locking of the model ENSO (see discussion in Wittenberg et al. 2006). The delayed occurrence of the mature phase in the CM2.1 simulation relative to observations is also evident in La Niña events.

The anomalous surface circulation associated with ENSO during the extended boreal winter season of December–March (DJFM) is illustrated by the patterns of regression coefficients of SLP versus standardized Niño-3 SST anomalies (Fig. 3). In the observed pattern (Fig. 3a), a deepened Aleutian low is seen over the NP, and a weak anomalous low pressure over central-western Atlantic near 35°N is discernible. In the CM2.1 simulation (Fig. 3b), the westward displacement of the anomaly over the NP relative to observations is likely related to the excessive westward spread of the simulated SST forcing in the tropical Pacific (Fig. 1) and the associated precipitation changes (Wittenberg et al. 2006). The
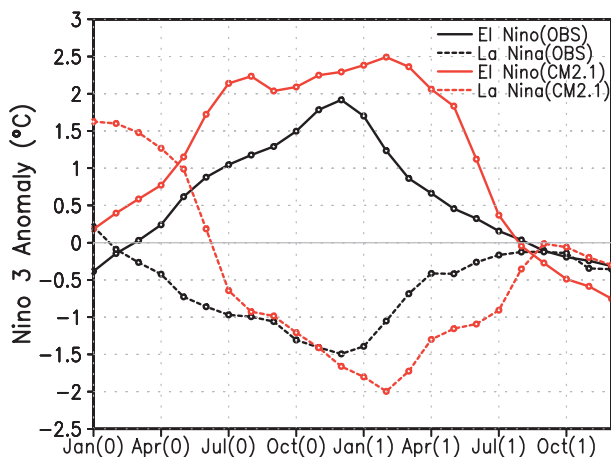
FIG. 2. Composite monthly evolution of the Niño-3 SST anomalies for El Niño (black solid curve) and La Niña (black dashed curve) events in observations, and El Niño (red solid curve) and La Niña (red dashed curve) events in the CM2.1 simulation. The abscissa represents a 24-month period from January of year(0) to December of year(1). A specific month in this period is identified by a label consisting of the first three letters of that month, followed by the year indicator (0 or 1) in parentheses. For instance, Dec(0) refers to the month of December in year(0).

simulated anomalous low over the NA extends farther eastward to eastern Europe. Caution may be needed when comparing the model and observational results over the western NA because the simulated anomalous low over the NP extends too far into the western NA.

To illustrate the seasonality of the SLP signal accompanying ENSO, the time evolution of the regression coefficients of SLP anomalies versus Niño-3 index over both the NP and NA sectors are shown in Fig. 4. For the NP sector (Figs. 4a,b), zonal variations are presented for averages over the latitudes between 35° and 55°N; for the NA sector (Figs. 4c,d), meridional variations are shown for averages over the longitudes between 70° and 20°W.

The observed negative anomaly in the NP region (Fig. 4a) is captured by CM2.1 (Fig. 4b), except that the simulated feature is more persistent in time, and maintains a stronger presence through March and April. The simulated anomaly position is also displaced westward by 15° of longitude.

Over the NA sector, the observed response in November and December (Fig. 4c) is characterized by a low pressure anomaly to the north and a weak high pressure anomaly to the south. This configuration is reversed in the January–April period, and the pressure pattern corresponds to the negative phase of NAO. Because the SLP pattern over the NA in December is almost opposite to that in January–March, averaging the pressure signals over the entire season (DJFM), as was done in computing Fig. 3a, leads to much weaker responses than the anomalies for individual months. The above seasonal dependence of the ENSO relationship with SLP over the NA sector is in agreement with Moron and Gouirand (2003), who analyzed a longer record of observational data (1873–1996). The negative
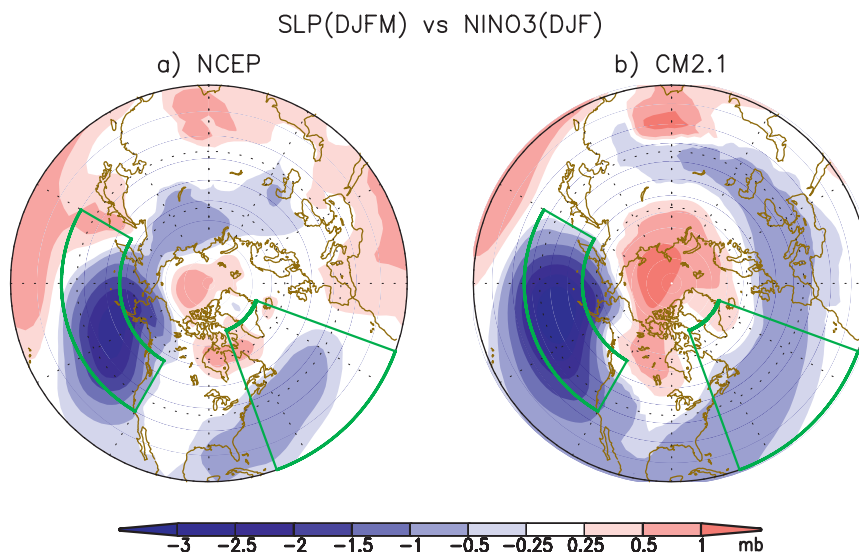

FIG. 3. Distributions of the regression coefficients of DJFM-mean SLP vs the standardized DJF-mean Niño-3 index based on the (a) NCEP–NCAR reanalysis and (b) CM2.1 simulation. Units: mb. Latitude and longitude ranges used for computing the zonal and meridional averages over the North Pacific (NP) and North Atlantic (NA) sectors (see Fig. 4) are indicated by green borders.
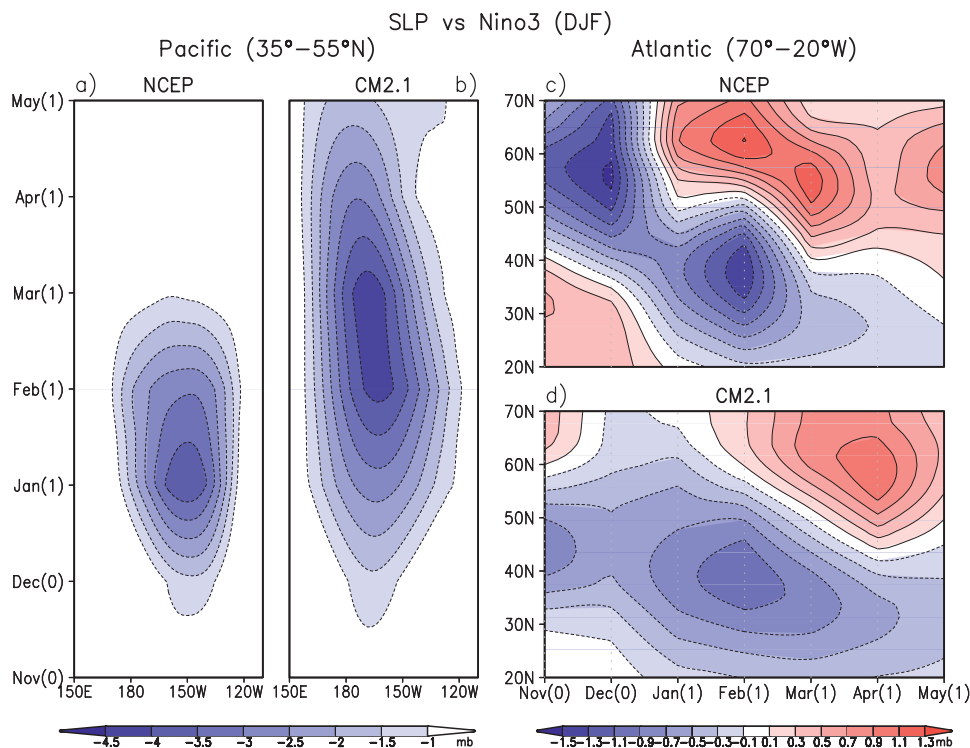
FIG. 4. (a),(b) Time–longitude and (c),(d) time–latitude variations of the regression coefficients of SLP anomalies vs standardized DJF-mean Niño-3 index, as computed using the (a),(c) NCEP–NCAR reanalysis and (b),(d) CM2.1 simulation. SLP anomalies are averaged (a),(b) meridionally over the 35°–55°N zone in the NP sector and (c),(d) zonally over 70°–20°W zone in the NA sector (see green outlines in Fig. 3). The contour intervals are 0.5 mb for (a),(b) and 0.2 mb for (c),(d).

NAO signal in response to El Niño during late winter is captured by the model (Fig. 4d). However, positive pressure anomaly in the high latitudes in the model atmosphere emerges in February, about one month later than the observations. In addition, the simulated positive anomaly peaks in April, about two months after the negative anomaly attains maximum amplitudes.

In view of the occurrence of the strongest observed NAO signals in January–February (JF), and the strongest simulated signals in February–March (FM), we shall hereafter define "late winter" as the JF period for the observations, and the FM period for the model. This slight difference in the definition of the later winter season for observed and model data is further motivated by the 1-month delay of the tropical Pacific SST forcing in CM2.1 relative to the observations, as illustrated in Fig. 2.

b. NAO variability and ENSO impact on the frequency of occurrence of its different phases

We next examine the NAO pattern in the observed and model atmospheres. The NAO pattern is defined as the leading EOF of the late winter (JF for observations and FM for the simulation) SLP field within the region

of 20°–70°N, 80°W–20°E, and is displayed in Fig. 5. Both the observed (Fig. 5a) and simulated (Fig. 5b) data exhibit a dipolelike pattern with centers of action at 40° and 65°N. The normalized temporal coefficients of the leading EOF of the SLP field serve as the NAO index. Outstanding NAO events correspond to those seasons with indices exceeding one standard deviation from normal.

Figure 6a shows density histograms of the normalized JF-mean NAO indices for the selected El Niño (red columns) and La Niña (blue columns) events during the period 1891–2008 (see Table 1). The NAO indices in this period are obtained using the 20thC dataset. This figure illustrates strong negative NAO indices (less than −1.0) are more frequent during El Niño years than during La Niña years. Conversely, strong positive NAO indices (greater than 1.0) are more frequent during La Niña years than El Niño years. The average values of NAO index during the observed 19 El Niño winters and 20 La Niña winters are −0.35 and +0.51, respectively. The difference between these composite values is statistically significant (p value = 0.008) using a t test.

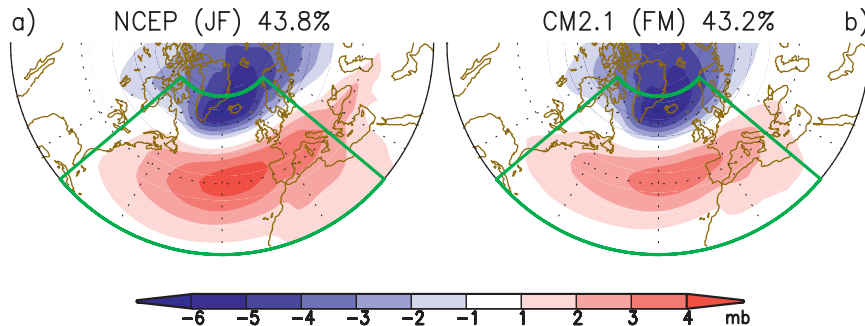The probability density functions (PDFs) of the normalized FM-mean NAO indices during El Niño winters

FIG. 5. The spatial pattern of the leading EOF of seasonal mean SLP over the NA sector (20°–70°N, 80°W–20°E, see green border), based on the (a) NCEP–NCAR reanalysis for the JF-mean season and (b) CM2.1 simulation for the FM-mean season. The patterns show the regression coefficients of seasonal mean SLP vs the standardized temporal coefficients of the EOF. Units: mb. The observed and simulated EOF modes account for 43.8% and 43.2% of the total variance, respectively.

(red curve) and La Niña winters (blue curve) in the CM2.1 simulation are compared in Fig. 6b. A pronounced shift in the distribution toward negative and positive NAO values are apparent for the El Niño and La Niña years, respectively, in agreement with observational results. The two distributions are statistically different (p value < 0.01) using a Kolmogorov–Smirnov test (Smirnov 1948). Statistically different composite values of the normalized NAO index are also found based on the simulated 252 El Niño winters and 215 La Niña winters (-0.40 vs $+0.33$, p value < 0.01). It is noteworthy that the difference between the composite NAO indices for El Niño and La Niña episodes exceeds 0.7σ in both observations and model. This difference may be sufficiently large to be of practical use in seasonal forecasting. It should also be noted that the magnitude of the composite NAO indices associated with El Niño winters is slightly stronger than that associated with La Niña winters in the CM2.1 simulation. This results is opposite to the results based on 20thC dataset, and previous observational studies (Pozo-Vázquez et al. 2001, 2005).

c. Observed and simulated surface climate response to ENSO and NAO in late winter

The link between ENSO and NAO is further explored by examining the surface climate signals in the North Atlantic–European sector associated with these two phenomena. The top four panels of Fig. 7 show the difference between the El Niño and La Niña composites of late-winter SLP, SAT, and precipitation, for both observations and model. These ENSO responses may be compared with the corresponding patterns based on differences between outstanding positive and negative NAO events, as shown in the bottom four panels.

The distribution of observed SLP for late winter (JF, see Fig. 7a) associated with ENSO shows a more distinct dipolelike pattern than the corresponding chart for the DJFM season (Fig. 3a). This dipolar pattern resembles the SLP pattern corresponding to the negative NAO phase (Fig. 7e). This dipolar feature is discernible in the corresponding SLP pattern in CM2.1 (Fig. 7b), although the simulated negative center over the extratropical NA is displaced westward relative to its observed counterpart. The amplitude of the dipolar anomaly is reduced in the simulation, as previously noted in Figs. 4c,d. The relatively weaker amplitude of SLP anomaly is possibly due to the very limited vertical resolution in the model stratosphere, so that El Niño teleconnection through the stratospheric pathway (e.g., Bell et al. 2009) is not well captured by the CM2.1 simulation. In addition, the relatively low horizontal resolution could also contribute to this weaker SLP response to ENSO in the North Atlantic–European region (Merkel and Latif 2002).

The ENSO-related responses of the SLP over NA depend linearly on the strength of both the warm and cold SST anomalies in the tropical Pacific (not shown). Thus, the nonlinear response to the amplitude of the El Niño anomaly over the eastern NA, as noted by Toniazzo and Scaife (2006) on the basis of reanalysis data, is not evident in the CM2.1 simulation.

Over NA, the dipolar SLP response to ENSO is associated with a quadruple pattern of SAT anomalies in both observations and model (Figs. 7a,b), with warming over eastern Canada–Greenland and southwestern Asia–northern Africa, and cooling over southeastern United States and northern Europe. These temperature signals bear a considerable resemblance to the negative NAO features as shown in Figs. 7e,f, and also compare well with those in previous observational studies (e.g., Hurrell 1996).

The model also reproduces the main features of the ENSO-related precipitation anomalies (Figs. 7c,d).

20thC
Histogram of the NAO index (JF)

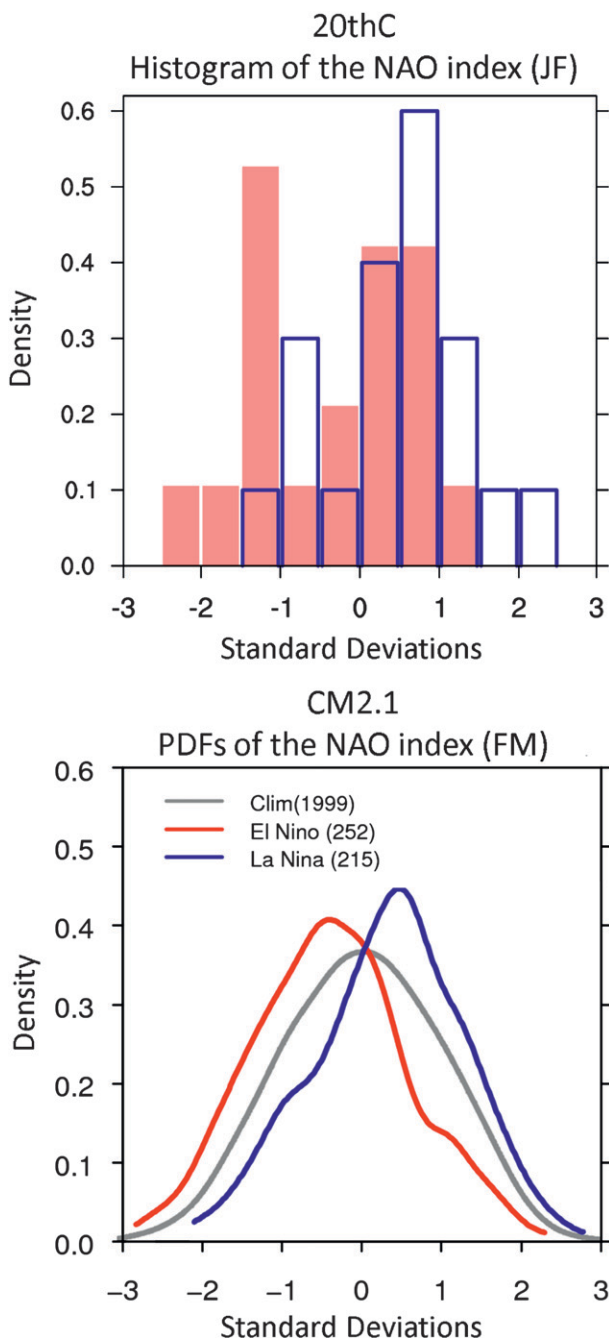## CM2.1
PDFs of the NAO index (FM)

FIG. 6. (a) Density histogram of the normalized JF-mean NAO indices for the selected El Niño winters (red-filled columns) and La Niña winters (blue unfilled columns) listed in Table 1 for the 1891–2008 period, as constructed based on the 20thC reanalysis. (b) PDFs of the normalized FM-mean NAO indices for the selected El Niño winters (red curve), La Niña winters (blue curve), and all winters (gray curve) in the CM2.1 simulation. The PDFs are obtained by a kernel density estimation.

Note in particular the wet band extending eastward from the California coast to southern Europe, as well as the dry conditions over northern Europe. This pattern of precipitation change resembles that associated with the NAO pattern (see Figs. 7g,h). The discrepancy between the observed and simulated precipitation signals over the west coast of Canada (Figs. 7c,d) is related to the prevalence of anomalous southerly (easterly) surface flow in that region, as inferred from the SLP patterns based on observational (model) data (Figs. 7a,b).

The above comparisons demonstrate a strong relationship between the surface climate anomalies accompanying ENSO and NAO, and the ability of CM2.1 in capturing this relationship. These findings lend credence to the model as a useful tool for investigating the mechanism for the teleconnection between ENSO and NAO.

4. Eddy–mean flow interaction in observed and simulated El Niño and La Niña events

a. Composites of mean flow and transient eddy intensity

Figure 8 shows the composites of 250-mb height and rms of bandpass-filtered 500-mb height for El Niño (left panels) and La Niña (right panels), as computed using the NCEP–NCAR reanalysis (first row), 20thC reanalysis (second row), and CM2.1 output (third and fourth rows). The results for "pure" El Niño years in the last row will be discussed later in this section. The composite pattern for 250-mb geopotential height (contours) during El Niño is characterized by a familiar wave train (Horel and Wallace 1981) over the Pacific–North American sector, with a negative anomaly over the southeastern United States extending farther eastward to the NA. As inferred geostrophically from the height field, the NP jet stream is strengthened in the subtropics and weakened in the extratropics during the El Niño events. The corresponding rms of filtered 500-mb height (shading in Fig. 8) is positively correlated with the strength of the westerly flow (i.e., eddy activity over the NP is enhanced at 30°N and suppressed at 50°N). Furthermore, the enhanced storm-track activity extends across the NA, with an axis that is oriented from southwest to northeast. This feature is consistent with the poleward deflection of the storm trajectory at the jet exit (Hoskins et al. 1983; Orlanski 1998). Such eastward extension of the storm tracks beyond the site of strengthening of the time-mean flow has been well documented in many observational and model investigations (e.g., Chang 1998; Seager et al. 2003; Lau et al. 2005; Seager et al. 2010). These studies noted that the ENSO-induced enhancement of the vertical and horizontal wind
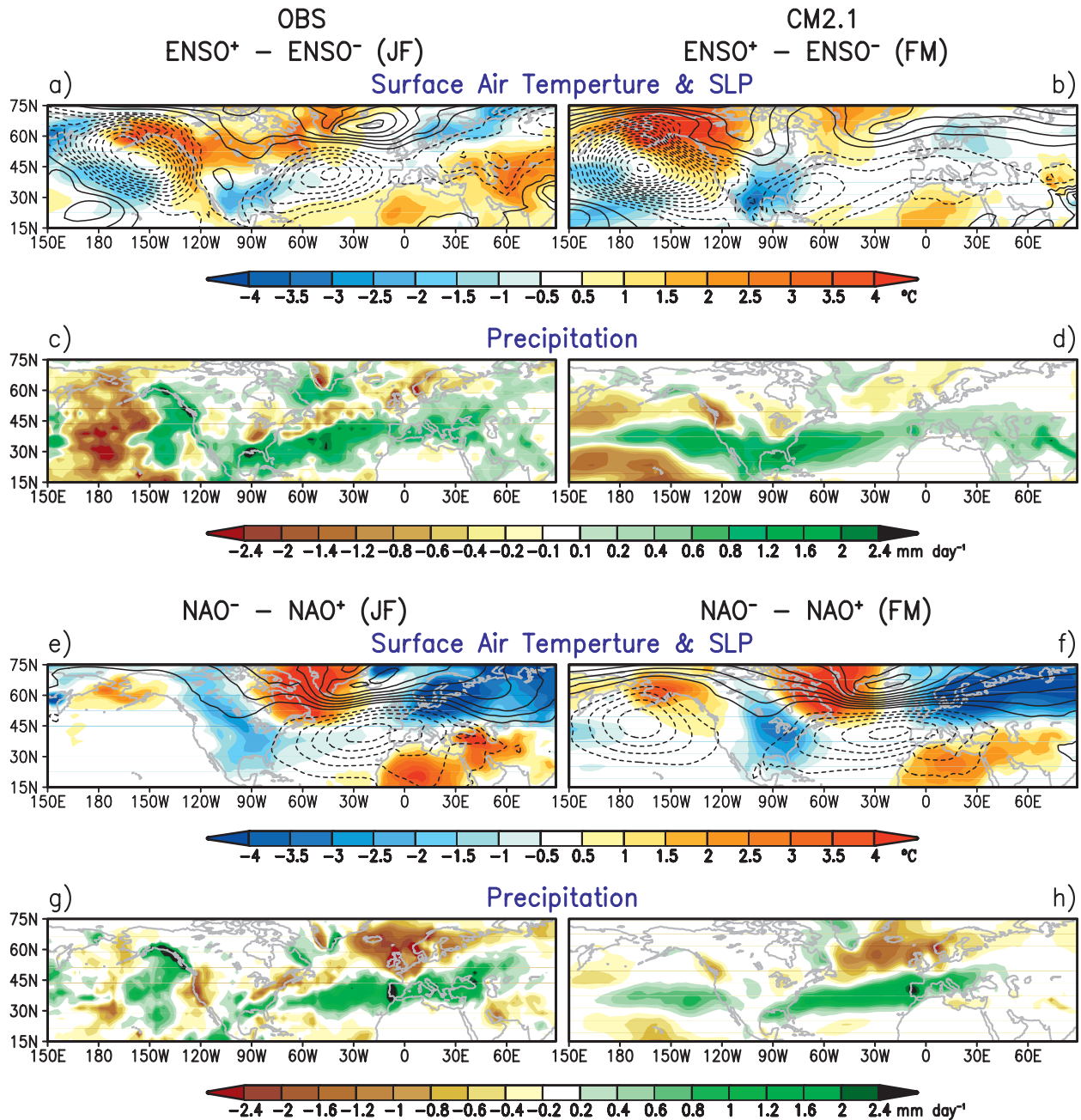
FIG. 7. Horizontal distributions of (a)–(d) El Niño minus La Niña composites and (e)–(h) NAO− minus NAO+ composites. The displayed fields are (first and third rows) surface air temperature (SAT; shading) and SLP [contours; intervals in (a),(b) and (e),(f) are 1 and 2 mb, respectively], and (second and fourth rows) precipitation. (left) Observations for the JF(1) period. (right) CM2.1 data for the FM(1) period. The observational results use the NCEP–NCAR reanalysis for SLP and SAT fields, and the GPCP dataset for precipitation. Observed (simulated) NAO± events are defined when the normalized JF(FM)-mean NAO indices exceed one standard deviation from normal.

shears in the vicinity of the jet stream could favor the development of transient disturbances, which propagate eastward and alter the pattern of eddy momentum fluxes farther downstream. The latent heat release within the precipitation zone along the NA storm track may also contribute to the maintenance of the eddy activity in that region (Hoskins and Valdes 1990).

Because of asymmetries in the tropical diabatic forcing in the two opposing phases of ENSO (Hoerling et al. 1997), both the observed and simulated wave trains in the
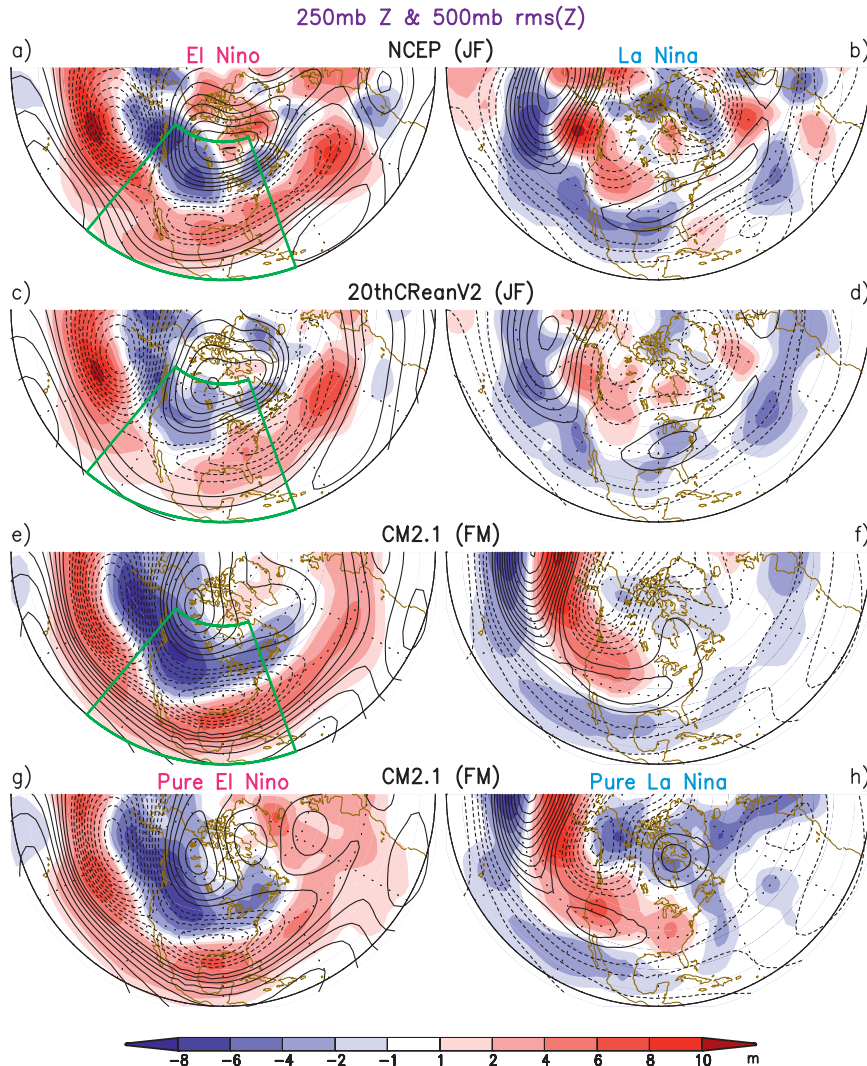
FIG. 8. Horizontal distributions of (left) El Niño and (right) La Niña composites of the 250-mb geopotential height (contours, interval: 10 m) and rms of the 2–10-day bandpass-filtered 500-mb geopotential height (shading, see scale bar at bottom). Results are shown for (a),(b) the NCEP–NCAR reanalysis and (c),(d) 20thC reanalysis for the JF(1) period, and (e),(f) for the CM2.1 simulation for the FM(1) period. (g),(h) Results show composites over pure El Niño (La Niña) events, which correspond to those episodes with DJF-mean Niño-3 index greater (less) than $+1.0\sigma$ (-1.0σ), but with only weak values of the FM-mean NAO index (i.e., between -0.2σ and $+0.2\sigma$). The outermost latitude circle represents 15°N. The regions used for the EOF of rms of filtered 500-mb height (see Fig. 10) are indicated by green borders in (a),(c), and (e).

La Niña events are displaced westward (right panels of Fig. 8) relative to their counterpart in the El Niño events (left panels of Fig. 8). The shading patterns in the right panels of Fig. 8 indicate that the NP storm track is shifted poleward in La Niña events.

b. Composites of **E** vectors and geopotential height tendencies

Figure 9 shows the anomalous **E** vectors and $\partial Z/\partial t$ (see definition in section 2c) in the same layout as Fig. 8.

The patterns of **E** in the El Niño composites show a continuous stream of eastward-directed **E** arrows along the enhanced storm track axis near 35°N, extending from the central NP to the NA sector in both observations and model (left panels of Fig. 9). These **E** patterns indicate enhanced eastward group propagation of the transient eddies relative to the mean flow.

At the eastern end of the Pacific storm track, there is a strong divergence of the **E** vectors for El Niño composites, with northeastward-directed arrows north of the

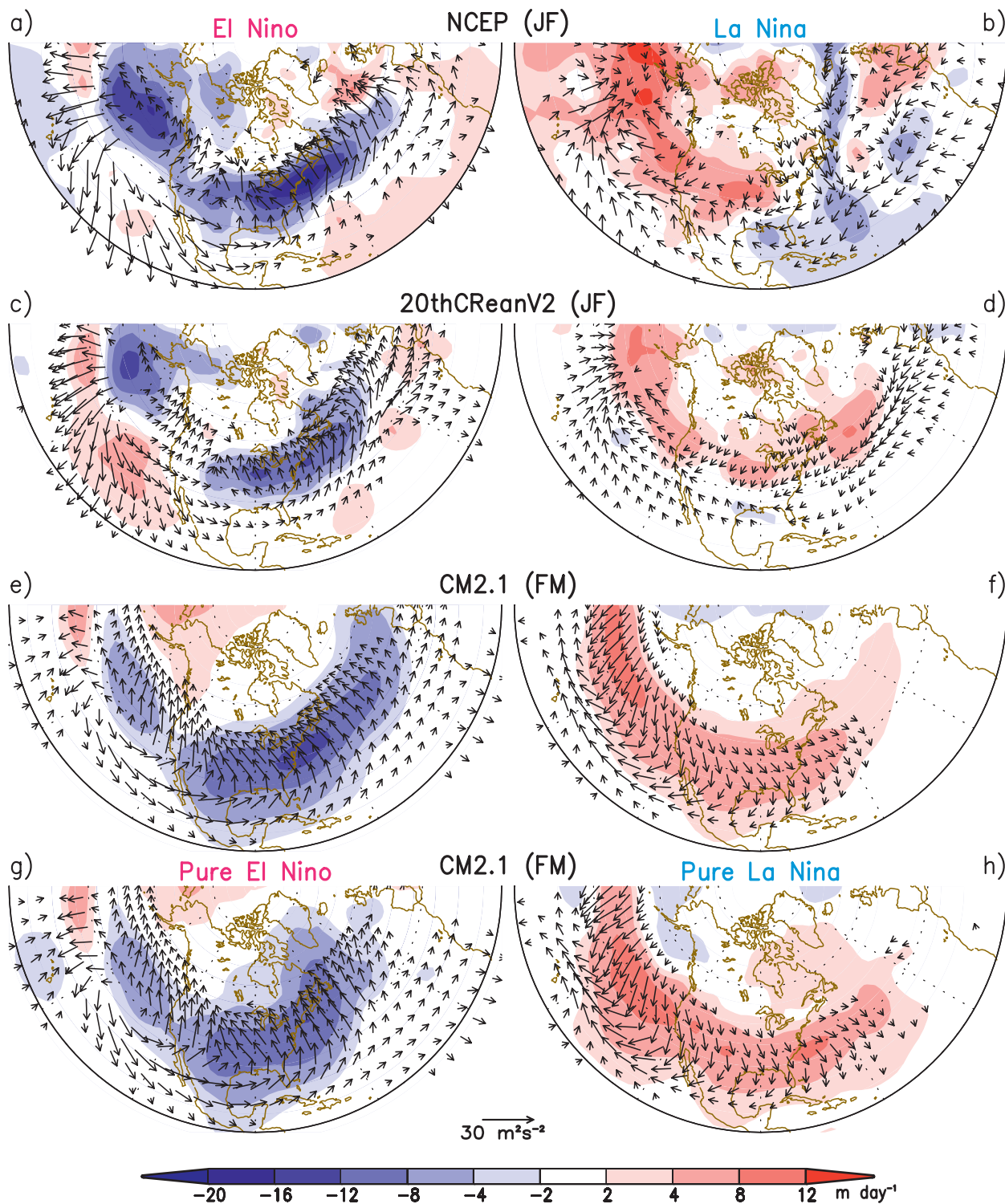FIG. 9. As in Fig. 8, but for 250-mb extended Eliassen–Palm **E** vectors (arrows, see scale at bottom) and eddy-induced height tendencies (shading, see scale bar at bottom). The **E** vectors with magnitude smaller than 3 m^2 s^{-2} are not plotted.

storm track, and southeastward arrows farther south. This pattern implies that the eddy momentum transport leads to acceleration of the westerly mean flow along the storm track (e.g., Trenberth 1986). The eddies therefore reinforce the subtropical westerly anomalies located south of the climatological jet, and maintain the deepened Aleutian low associated with El Niño.

Farther downstream over the western and central Atlantic, the anomalous **E** vectors are mostly directed poleward. This pattern is associated with divergence of **E** and zonal wind acceleration along 30°N, and convergence of **E** and zonal wind deceleration along 50°N. The cyclonic curvature of **E** in midlatitude NA is indicative of northward wind acceleration (e.g., Trenberth 1986). The above configuration of zonal and meridional wind changes is conducive to negative height tendencies in the temperate zone of the NA.

The composite $\partial Z/\partial t$ during El Niño winters (shading in left panels of Fig. 9) shows negative $\partial Z/\partial t$ to the north of the equatorward shifted storm track, with one center located southeast of the Aleutian Islands, and another prominent feature extending from the east coast of North America to the midlatitude NA. The negative $\partial Z/\partial t$ pattern over the NA is in accord with the above-mentioned divergence and curl of **E** over that region. Comparison between the spatial pattern of Z (left panels of Fig. 8) and that of $\partial Z/\partial t$ (left panels of Fig. 9) reveals that the transient eddies act to maintain the upper-tropospheric negative height anomalies over the Aleutians and the southeastern United States. This finding is consistent with previous studies highlighting positive feedback between transient eddy vorticity flux and the extratropical atmospheric response to tropical SST anomalies (Held et al. 1989; Branstator 1995; Kushnir et al. 2002; Orlanski 2005). The amplitude of these negative $\partial Z/\partial t$ anomalies over the NP is lower in CM2.1 simulation than in observations. The weaker eddy forcing in the model atmosphere may be related to the relatively low horizontal resolution of CM2.1.

Most interestingly, substantial eddy vorticity forcing is discernible over the NA region, with spatial extent and amplitude being larger than that over the NP region. This coherent eastward extension of eddy forcing from the NP sector has not yet been emphasized previously in the literature.

The pattern of simulated meridional eddy heat flux $\overline{v'T'}$ at 850 mb (not shown) during El Niño winters is characterized by a prominent maximum along the enhanced storm-track axis near 35°N, and extending from the central NP to the NA. This pattern indicates strong heat flux convergence poleward of the storm-track axis, and is associated with positive geopotential height tendency in the upper troposphere and negative tendency

near the surface (Lau and Nath 1991). Although baroclinic effects of eddy heat flux tend to offset the barotropic effects of the eddy vorticity flux in the upper troposphere, the latter is stronger than the former by 50%–80% (Lau and Nath 1991). Thus, the net eddy-induced $\partial Z/\partial t$ at the 250-mb level can still be as large as 6–10 m day^{-1} over the midlatitude NA. The characteristic time scale of the eddy forcing, as estimated from the ratio of the amplitudes of the height anomaly (left panels of Fig. 8) to those of the $\partial Z/\partial t$ (left panels of Fig. 9), is about 6–10 days over the western Atlantic. In the lower troposphere, due to the cooperation between the forcing associated with heat and vorticity fluxes (Lau and Holopainen 1984; Lau and Nath 1991), the eddy forcing could be even more efficient in producing the negative SLP tendencies at 30°–50°N over NA.

Inspection of the La Niña composites in the right panels of Fig. 9 indicates that the eastward-directed **E** vectors along the poleward-shifted storm tracks, as simulated by CM2.1 (Fig. 9f), is not evident in the observations. However, there still exist some common features between observations and model. For example, westward-directed and convergent **E** vectors are found along the belt of suppressed synoptic variability over the NP near 30°N, where zonal wind deceleration occurs. Moreover, the anticyclonic curvature of **E** (and implied southward acceleration) over the central NP and North America is consistent with the local $\partial Z/\partial t$ pattern. The positive center of $\partial Z/\partial t$ over the central Pacific is displaced to the west of its El Niño counterpart, indicating that the transient feedback contributes to the maintenance of the asymmetric height response (cf. left and right panels of Fig. 8). This zone of positive $\partial Z/\partial t$ also extends eastward to the western Atlantic, and is coincident with the positive height anomaly in that region during La Niña winters.

c. ENSO response after removal of NAO signal

To exclude the contribution of NAO-related eddy forcing from the model composites displayed in Figs. 8–9, the composites are also constructed using an alternate set of pure ENSO years. Pure El Niño (La Niña) correspond to those episodes with DJF-mean Niño-3 index greater (less) than $+1.0\sigma(-1.0\sigma)$, but with only weak values of the FM-mean NAO index (i.e., between -0.2σ and $+0.2\sigma$). There are 42 and 36 winters in the CM2.1 simulation satisfying the criteria for pure El Niño and pure La Niña, respectively. The results are displayed in the last row of Figs. 8–9.

Since the simulated geopotential height anomalies based on all El Niño and La Niña events are weak over the eastern Atlantic (see contours in Figs. 8e,f), it is thus not surprising that the changes of the geopotential height anomalies is not very dramatic, except for the

slightly reduced amplitude over the western Atlantic (see contours in Figs. 8g,h). This negative geopotential height anomaly over the western NA maintains the southward-shifted storm track over that site and locations farther east (see shading in Figs. 8g,h). Thus, although the eddy-induced height tendency shows less penetration into the eastern NA, its amplitude over the western NA is still substantial and comparable to those in Figs. 9e,f. This result confirms that ENSO influences over the western NA are substantial even after the removal of the NAO-related contributions. Hence, we conclude that ENSO can influence the storm track and transient eddy forcing over the western NA region irrespective of the strength of NAO.

d. Storm-track variations over North America and its relationship to both ENSO and NAO

The spatial distributions of storm-track intensity (shading in Fig. 8) show distinct meridional shifts in the zone of maximum transient eddy activity over southern United States–Gulf of Mexico and the Pacific Northwest during ENSO events. These findings are consistent with the recent results of Seager et al. (2010), who showed that waves propagate along a more southern path toward southwestern North America during El Niño, while they take a more northward route toward the Pacific Northwest during La Niña. To depict such interannual variations of the site of eddy activity over the North American sector, we perform an EOF analysis of the rms of filtered 500-mb height field over the region 15°–60°N, 130°–70°W (see boxed area in Fig. 8) in late-winter season for both observations and model.

The first or second EOF mode based on all three datasets examined here (Fig. 10) is dominated by a center over northwestern North America, and another center of the opposite polarity over the southern United States and the Gulf of Mexico. The patterns in Fig. 10 compare well with the El Niño composites of rms amplitudes over North America (shading in the left panels of Fig. 8).

The temporal coefficients of the EOF patterns presented in Fig. 10 represent the variations in the strength and location of the storm path over North America. We shall henceforth refer to this time series as the storm path index (SPI). The temporal correlation coefficients among the SPI, ENSO, and NAO indices are displayed in Table 2. It is evident that the correlation coefficients between SPI and both ENSO and NAO indices (see bottom two rows of Table 2) are not only highly significant (p value < 0.05) for each dataset, but also much higher than the linear correlation between ENSO and NAO indices (see top row of Table 2). This finding signifies that the storm-track anomaly over North America plays a crucial role in the linkage between ENSO and

NAO. In view of the three-way relationship between SPI, ENSO, and NAO, the partial correlation coefficient (e.g., Spiegel 1988; see the appendix for details) between ENSO and NAO is computed using CM2.1 data, with the contribution from SPI being removed from both ENSO and NAO. This procedure yields a partial correlation coefficient of 0.06, which is noticeably smaller than the corresponding value (i.e., −0.2, with a p value < 0.01, see top-right entry of Table 2) as obtained without removal of SPI contribution. This partial correlation analysis suggests that ENSO would have almost no impact on NAO if the storm-track variability over North America were removed.

5. Simulation of the ENSO–NAO relationship with an atmospheric GCM

To further demonstrate the impacts of tropical Pacific SST forcing on the atmospheric variability in the NA sector, as alluded to in the previous section, three experiments with AM2.1 (atmospheric component of CM2.1) are carried out:

- a 30-yr control experiment (CTRL) in which the 2000-yr-averaged climatological seasonal cycle of the SST field generated in the CM2.1 simulation is imposed at the lower boundary at all ocean grid points;
- an El Niño experiment (ELNO);
- a La Niña experiment (LANA).

The latter two experiments differ from the CTRL experiment only in the prescription procedure of the SST field in the tropical Pacific. Monthly-averaged composite El Niño (La Niña) anomalies are obtained from composites of El Niño (La Niña) events identified in the 2000-yr simulation with CM2.1. The composite monthly SST anomaly in the tropical Pacific (15°S–15°N, 135°E to the American coasts) from March(0) to November(1) is then added to the climatological mean seasonal cycle. All anomalies outside of the tropical Pacific are masked out. A 30-member ensemble of the 21-month [March(0)–November(1)] integrations is performed separately for the composite El Niño forcing and La Niña forcing scenario. Within each ensemble, the individual members are initiated from independent conditions as extracted from various years in the 30-yr-long CTRL experiment. The design of these experiments is very similar to that used in Lau and Nath (2009), to which the readers are referred for further details. In the following analysis, the anomalous response of AM2.1 to composite SST forcing prescribed in tropical Pacific region is obtained by subtracting the 30-yr average of the CTRL run from the 30-member ensemble mean of the ELNO or LANA experiment.

a) NCEP (JF) EOF1 17.5%

b) 20thC (JF) EOF2 14.0%
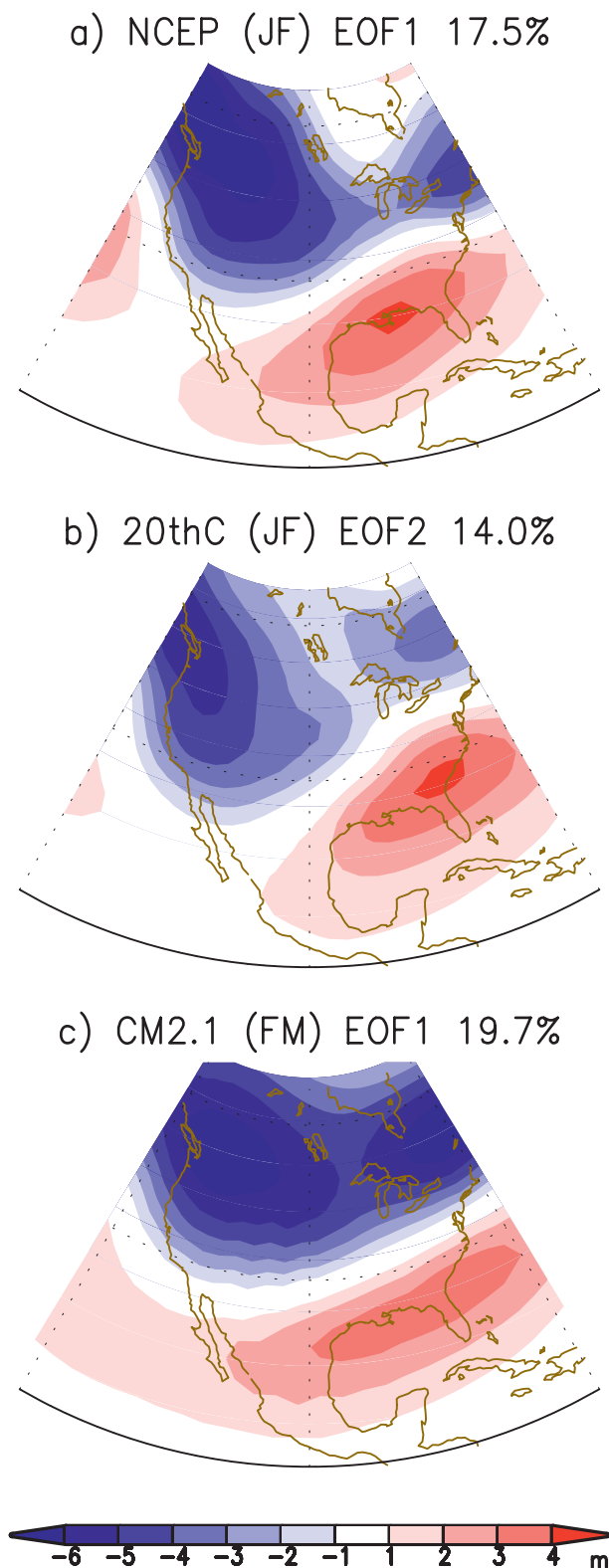

c) CM2.1 (FM) EOF1 19.7%

FIG. 10. The spatial pattern of the (a),(c) first and (b) second EOF of the seasonal mean normalized rms of filtered 500-mb height field over the North American sector (15°–60°N, 130°–70°W) based on the (a) NCEP–NCAR reanalysis for the JF-mean season, (b)

TABLE 2. Temporal correlation coefficients among indices for the DJF-mean Niño-3, the late-winter NAO, and the late-winter storm path index, as computed using the NCEP–NCAR reanalysis, 20thC reanalysis, and the CM2.1 simulation. The storm path index (SPI) is defined as the temporal coefficients of the EOF patterns presented in Fig. 10 (see text in section 4d for details). Values exceeding the 95% significance level are given in bold. The p values as estimated by applying a two-tailed Student's t test are given in parentheses. Degrees of freedom are estimated following that outlined in footnote 1 of Lau and Nath (2004). Specifically, the spectra for the simulated and observed ENSO indices [Fig. 19 of Wittenberg et al. 2006] suggest that typical period of an ENSO "cycle" in both simulated and observed system is approximately 4 yr. Given that there are 2 degrees of freedom in each ENSO, we assume that 2 yr of data are required to yield 1 degree of freedom.

	NCEP–NCAR	20thC	CM2.1
Niño-3 vs NAO (p value)	−0.15 (0.4)	−0.19 (0.14)	**−0.20**(<0.01)
SPI vs Niño-3 (p value)	**0.61**(<0.01)	**0.53**(<0.01)	**0.54**(<0.01)
SPI vs NAO (p value)	**−0.38**(<0.01)	**−0.27**(0.04)	**−0.46**(<0.01)

Figure 11 shows the FM-mean ELNO (left) and LANA (right) response in 250-mb geopotential height (contours), rms of filtered 500-mb height (shading in Figs. 11a,b), **E** (arrows), and $\partial Z/\partial t$ (shading in Figs. 11c,d). The ELNO and LANA experiments reproduce the teleconnection pattern associated with El Niño and La Niña events based on CM2.1 (Figs. 8e,f) remarkably well. Most strikingly, the 250-mb height response in ELNO experiment (Fig. 11a) is characterized by a negative NAO pattern with below-normal heights extending eastward from the southeastern United States to NA, and above-normal heights extending from western Canada to southern Greenland. The polarities of these anomaly centers are reversed in LANA experiment (Fig. 11b). These results indicate that much of the 250-mb height changes on the interannual time scale may be attributed to tropical Pacific SST forcing alone.

Patterns of the storm track, **E**, and $\partial Z/\partial t$ also bear a considerable resemblance to those in Figs. 8e,f and Figs. 9e,f. These results are consistent with the model study of Seager et al. (2010), who demonstrated that changes in eddy propagation in the Pacific–North American sector during ENSO events can be generated by tropical Pacific

←

20thC reanalysis for the JF-mean season, and (c) CM2.1 simulation for FM-mean season. The patterns show the regression coefficients of seasonal mean rms of filtered 500-mb height vs the standardized temporal coefficients of the EOF. Units: m. The fraction of variance explained by each EOF mode is given at the top of (a)–(c).
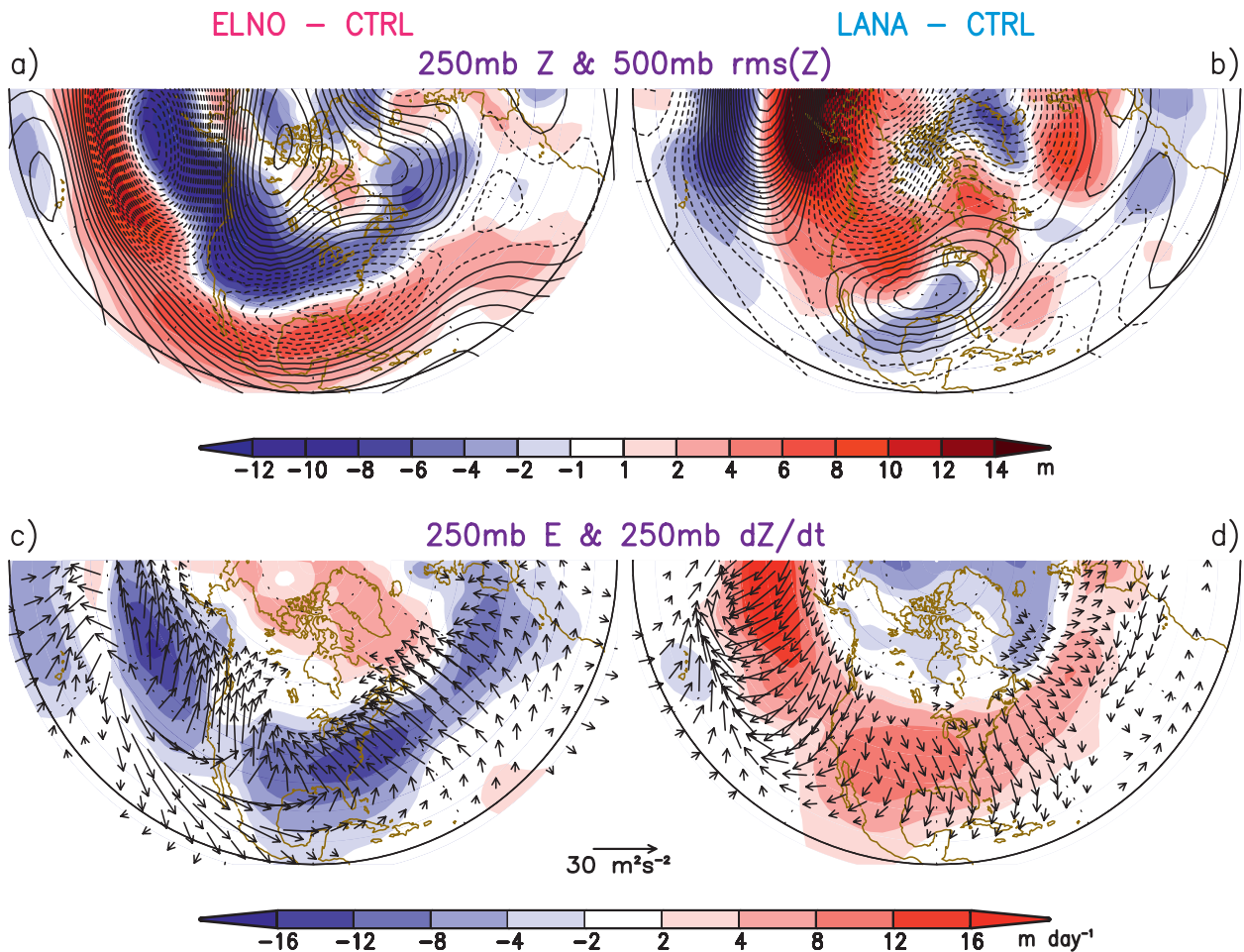
FIG. 11. (a),(b) As in Figs. 8e,f and (c),(d) as in Figs. 9e,f, but for results based on responses in (left) ELNO and (right) LANA experiments. Results are obtained by subtracting the data for the CTRL experiments from the output of the ELNO or LANA experiments.

SST forcing alone. Our results further indicate that the changes in transient eddy forcing over the NA sector are also linked to ENSO-related SST anomalies in tropical Pacific.

Although the patterns of the height anomalies in ELNO and LANA runs (Figs. 11a,b) resemble those in the El Niño and La Niña composites based on output from the fully coupled simulation (Figs. 8e,f), the amplitudes in the former are generally higher than those in the latter. These results could be due to the absence of oceanic negative feedback on surface heat flux forcing in the midlatitude in the AGCM simulation (Lau and Nath 1996). Moreover, since there is no two-way air–sea coupling in both the tropical Indian and Atlantic Oceans in the AGCM simulation, the difference between AM2.1 and CM2.1 results could also be attributed to the remote SST forcing originating from these ocean basins, which could amplify or reduce the midlatitude atmospheric response (e.g., Alexander et al. 2002; Annamalai et al. 2007). As noted in Annamalai et al. (2007), height anomalies forced by Indian Ocean SST anomalies are opposite to those forced by tropical Pacific SST anomalies over the PNA region. In the hybrid coupled models like the Tropical Ocean and Global Atmosphere-Mixed Layer (TOGA-ML) model described by Lau and Nath (1996), where the tropical SST variability is specified but the midlatitude atmosphere is coupled to a mixed-layer ocean model, the midlatitude oceanic responses to atmospheric driving could exert positive feedbacks on the atmosphere. Further investigation of these issues, and especially the relative importance of the different factors involved, would require additional simulations with coupling being confined to extratropical and tropical ocean basins, either separately or in combination with each other. Such investigation is beyond the scope of this study.

6. Circulation patterns and SST environment associated with various combinations of ENSO and NAO phases

The covariability of ENSO and NAO events can be summarized by the scatter graph shown in Fig. 12, in which the data for each winter season in the 2000-yr simulation are indicated by a dot, with abscissa and ordinate corresponding to the normalized FM-mean NAO index and DJF-mean Niño-3 index, respectively. Despite the weak (but nonetheless statistically significant) overall correlation of −0.20 between the ENSO and NAO indices, we have presented ample evidence in the previous sections on the preferred occurrence of negative NAO events during El Niño, and positive NAO events during La Niña. It is hence of interest to study in more detail the circulation characteristics in those winter seasons with strong positive indices in ENSO and strong negative indices in NAO (see red dots in top-left quadrant of Fig. 12; hereafter labeled as ENSO+/NAO−), as well as strong negative indices in ENSO and strong positive indices in NAO (ENSO−/ NAO+; see red dots in bottom-right quadrant). The threshold for identifying strong indices is one standard deviation from normal. These two subgroups of winters conform to the ENSO–NAO relationship documented in the previous sections, and are referred as the "strong combinations." It is also of interest to contrast the behavior in these strong combinations against that in the winters with strong positive ENSO and NAO (ENSO+/NAO+; blue dots in top-right quadrant of Fig. 12), or with strong negative NAO and ENSO (ENSO −/NAO−; blue dotes in bottom-left quadrant). The latter two subgroups do not conform to the ENSO–NAO relationship noted earlier, and are referred as the "weak combinations." In accord with the PDF distributions in Fig. 6b, the number of winters in the weak combinations is considerably fewer than that in the strong combinations (see population counts shown at the four corners of Fig. 12). For example, in late winter it is 2–3 times more likely to have a strong negative NAO during El Niño events than a strong positive NAO. Similarly, a strong positive NAO is 2–3 times more likely to occur than a strong negative NAO during La Niña events.

Our main goal in this section is to contrast the spatial patterns of the circulation and storm-track activity occurring in each of the four combinations described above, and to study the possible factors contributing to the differences among the composites based on these categories. The limited observational record precludes a parallel analysis of the events occurring in the real climate system.
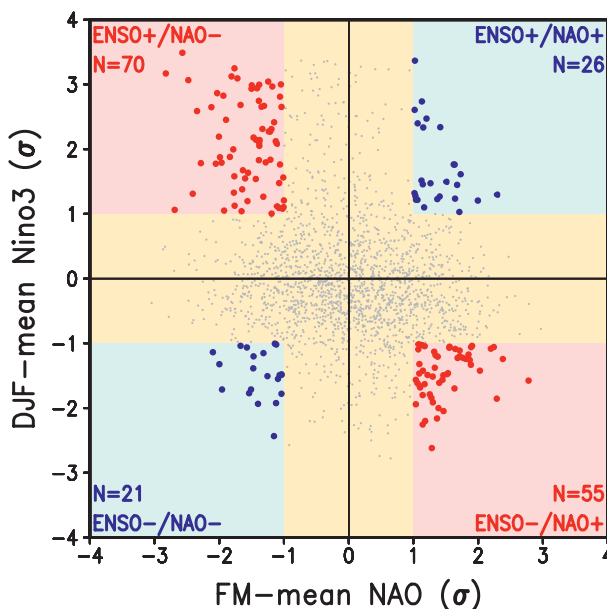

FIG. 12. Scatterplot of normalized DJF-mean Niño-3 index vs normalized FM-mean NAO index for the 2000-yr CM2.1 dataset. The abscissa (ordinate) of each dot in this diagram represents the amplitude and sign of the NAO (Niño-3) index for an individual winter season. Both weak ENSO and NAO winters (i.e., all winters in the yellow region) are displaced with small gray dots. Red and blue dots indicate the four subgroups with strong Niño-3 and NAO indices. Red dots represent the cases of "strong combination," and blue dots are the cases of "weak combination." These four subgroups of cases are selected for constructing composites in Fig. 13. The number of events for each subgroup is shown at the four corners.

a. Mean flow and transient eddy intensity in the "strong" and "weak" combinations

Figure 13 presents composite geopotential height anomalies and rms of filtered 500-mb height fields, as constructed based on the four types of combinations among the ENSO and NAO indices. As expected from the definition of the ENSO+/NAO− and ENSO−/NAO+ categories, the 250-mb height anomaly patterns for the strong combinations (Figs. 13a,d) exhibit a distinct zonally symmetric character, with out-of-phase variations between anomalies at 40°N and those in the Arctic zone. As compared to the composites based on the ENSO index (Figs. 8e,f), the features in Figs. 13a,d are extended much more eastward to the eastern Atlantic and Europe. The patterns in Figs. 13a,d are also similar to the height anomaly pattern during and after the mature phase of the seesaw between Aleutian and Icelandic lows, as presented by Honda et al. (2001). The rms of filtered 500 mb for the strong combinations also exhibit elongated positive anomalies along 35°N in ENSO+/NAO− (Fig. 13a) and 60°N in ENSO−/NAO+ (Fig. 13d). The zonally
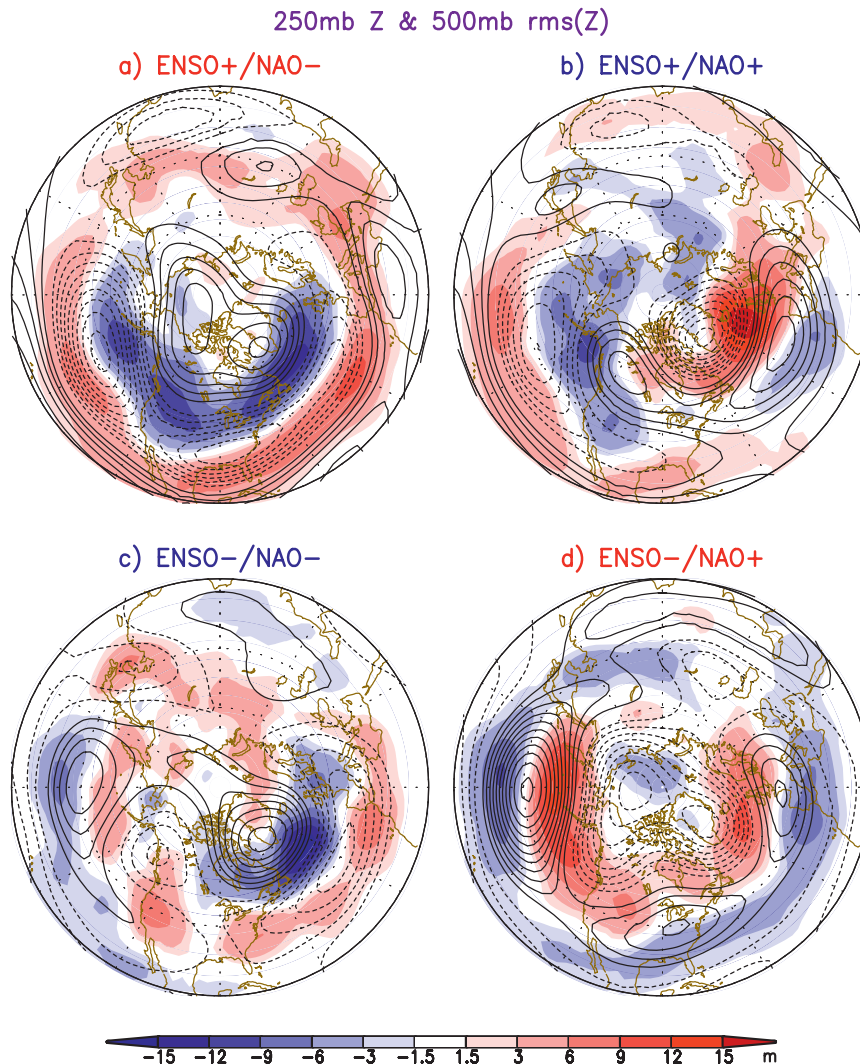
250mb Z & 500mb rms(Z)

FIG. 13. Composites of 250-mb geopotential height (contours, interval: 15 m) and rms of the bandpass-filtered 500-mb geopotential height (shading, see scale bar at bottom) for the FM(1) period. Composites are shown for the subgroups of (a) ENSO+/NAO−, (b) ENSO+/NAO+, (c) ENSO−/NAO−, and (d) ENSO−/NAO+ in the CM2.1 simulation. The outermost latitude circle represents 20°N.

extended nature of the rms patterns in these panels suggests a possible linkage between the Pacific and Atlantic storm tracks in those winters.

In contrast, the height patterns in the weak combinations (Figs. 13b,c) are characterized by a much stronger degree of zonal asymmetry. The associated storm-track activities appear to be organized on a smaller regional scale (i.e., over the NP and NA basins separately). It is also noticeable that the height anomaly center over the NP in the strong combinations is stronger as compared to the corresponding weak combinations.

The relatively larger number of strong combinations events suggests a preference for the circulation

anomalies to be more zonally symmetric during ENSO events. Seager et al. (2003) have also noted that ENSO forcing exerts a significant impact on the zonally symmetric extratropical circulation in winter and spring.

b. Dynamical mechanism

The question that may be raised, then, is how could the transient disturbances maintain their intensity near the decay region at the eastern end of the Pacific storm track during the winters with a strong combination. Figure 14 shows the (ENSO+/NAO−) minus (ENSO+/NAO+) composites of FMA-mean SST and precipitation in CM2.1. April is included in the composite in
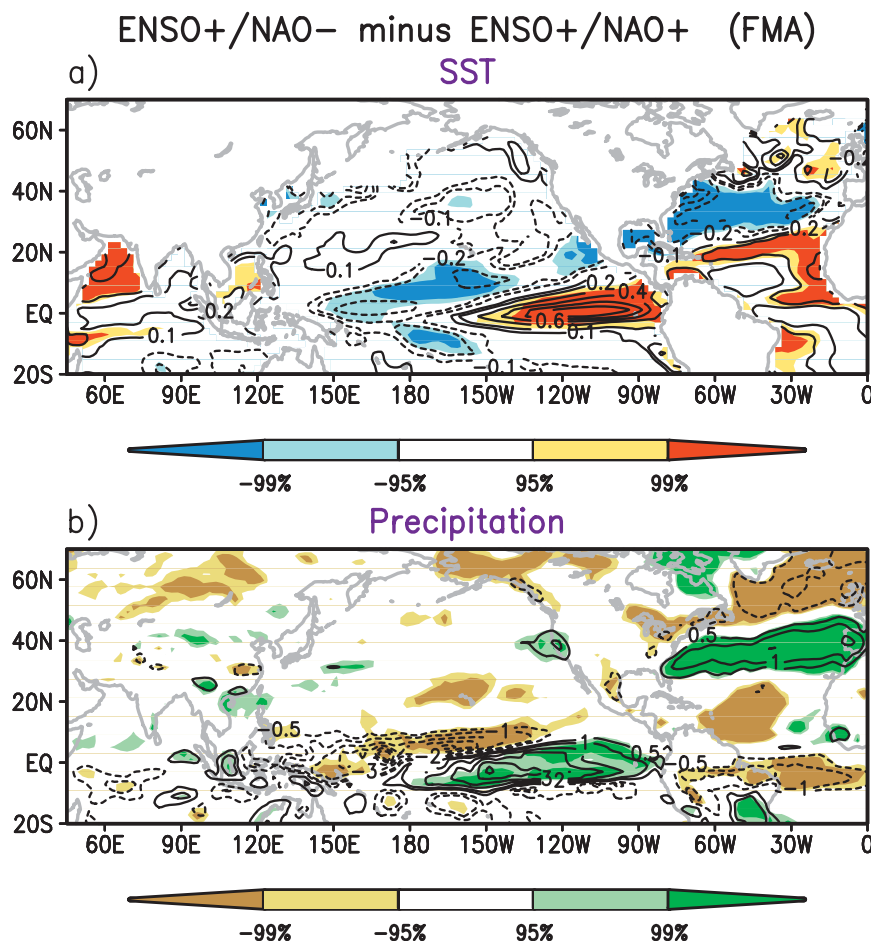
ENSO+/NAO− minus ENSO+/NAO+ (FMA)

FIG. 14. The (ENSO+/NAO−) minus (ENSO+/NAO+) composites of (a) SST (units: °C) and (b) precipitation (units: mm day^{-1}) for the FMA(1) period, as computed using the CM2.1 simulation. SST in (a) is contoured at ±0.1, ±0.2, ±0.4, ±0.6, ±0.8, and ±1.0. Precipitation in (b) is contoured at ±0.5, ±1.0, ±2.0, ±3.0, and ±4.0. Shading indicates the regions of the 95% and 99% confidence levels by using a two-tailed Student's t test.

view of the fact that the tropical Atlantic exhibits a delayed warming relative to that in the Pacific.

In ENSO+/NAO− winters, the warm SST anomaly in the eastern equatorial Pacific is significantly stronger than that in ENSO+/NAO+ winters (Fig. 14a). The precipitation (and the accompanying condensational heating) in ENSO+/NAO− winters is also relatively stronger over the central and eastern Pacific (Fig. 14b). Thus, the baroclinicity near the surface and the lower troposphere are expected to strengthen over the central and eastern Pacific in ENSO+/NAO− winters. Similar increased baroclinicity in the mideastern Pacific has been noted in Orlanski (2005) for El Niño winters. He argues that the reduced amplitude of the eastern Pacific ridge in El Niño winters is associated with the generation or regeneration of baroclinic waves in the mideastern Pacific, which tend to break cyclonically and

produce a trough tendency. Our study indicates that the enhanced subtropical baroclinicity over the central and eastern tropical Pacific could be a possible explanation for the eastward penetration of the NP storm track to the southern United States in ENSO+/NAO− winters.

The east–west dipolar pattern of the SST anomalies in Fig. 14a resembles the second EOF pattern of the tropical Pacific SST (not shown). The averaged value of the normalized temporal coefficients of this second EOF are 1.21 and 0.65 for the ENSO+/NAO− and ENSO+/ NAO+ subgroups, respectively. The significant difference between these two composite values of the EOF coefficients (p value = 0.02) suggests that the El Niño events in ENSO+/NAO− winters are characterized by enhanced SST warming in the eastern equatorial Pacific, whereas ENSO+/NAO+ winters are associated with warming in the central Pacific.

SST anomalies in other ocean basins may also modulate the ENSO signal over the North Atlantic–European region. For instance, it has been suggested that when SST anomalies over the tropical North Atlantic and tropical eastern Pacific are both warm, the SLP response is amplified and consistent with the negative phase of NAO (e.g., Gouirand and Moron 2003; Mathieu et al. 2004). It has also been noted that ENSO-related SST anomalies over the Indo-Pacific region can contribute to the long-term trend in NAO (e.g., Hoerling et al. 2001). Furthermore, low-frequency variability of SST anomalies in the western boundary current regions (i.e., Gulf Stream) may also influence the storm track and circulation over the NA during ENSO events (Kwon et al. 2010). Further study is needed to delineate the modulation of ENSO signal over the North Atlantic–European region by SST anomalies beyond the tropical Pacific.

Figure 14b shows stronger positive precipitation anomalies near 30°N over the NA in ENSO+/NAO− than that in ENSO+/NAO+. The enhanced latent heat release in this site could lead to stronger growth of the disturbances along the equatorward-shifted storm track in the ENSO+/NAO− cases. Hoskins and Valdes (1990) have also noted the importance of diabatic heating in maintaining the low-level baroclinicity, which in turn supports the development of transient eddies.

7. Summary and discussion

The mechanisms contributing to the tropospheric teleconnection between ENSO and NAO are examined based on a multicentury integration with a coupled GCM. The model captures well the observed features of both ENSO and NAO responses at the surface in late winter. The relationship between ENSO and NAO has a distinct seasonal dependence in both observations and model. The negative NAO phase occurs more frequently in late winter during El Niño events, and the positive NAO phase occurs more frequently in La Niña events. The model output exhibits a 1-month delay in the emergence of the NAO signals. This discrepancy may be related to the postponement of the ENSO mature phase in the simulation.

We investigated the mechanism of this ENSO–NAO relationship by examining the role of transient eddy forcing over the North Atlantic–European region. The negative 250-mb height anomaly over the NP is part of a stationary Rossby wave train forced by SST changes in the tropical Pacific during El Niño events. The strengthened zonal flows on the equatorward flank of this height anomaly enhance the development of synoptic-scale disturbances. In those El Niño events with strong SST warming in the equatorial Pacific, the storm-track

disturbances remain active over the eastern portion of the subtropical NP due to the strengthened meridional SST gradient over that site. As these transient fluctuations reach the Atlantic storm-track region, they induce negative $\partial Z/\partial t$ over the region corresponding to the southern lobe of NAO. Many of the model results are verified by two independent reanalysis datasets. The simulation of these eddy effects in the ELNO and LANA experiments using AM2.1 provides further evidence that ENSO-related SST anomalies in the tropical Pacific play a significant role in modulating eddy–mean flow interactions over the NA sector.

The characteristic patterns of storm-track variability over North America associated with ENSO are themselves the principal modes of storm-track variability in both NCEP–NCAR reanalysis and CM2.1. The corresponding principal component is significantly correlated with both ENSO and NAO indices in each dataset. This result suggests the role of the storm-track anomaly over the North America in the linkage between ENSO and NAO.

The following processes may contribute to the seasonal dependence of the ENSO–NAO relationship documented in this study:

- Aleutian low and Icelandic low seesaw
  The time evolution of the regression coefficients of SLP anomalies versus ENSO (Fig. 4) is consistent with the formation of the SLP seesaw between Aleutian low (AL) and Icelandic low (IL), as described by Honda et al. (2001). In particular, their results show that the out-of-phase relationship between the intensity of AL and IL during the late winter (February to mid-March) is preceded by weak in-phase association during early and midwinter (November–December). This seesaw is initiated by the amplification of the AL anomalies due to wave-activity accumulation in early and middle winter. Then the propagation of a Rossby wave train across North America leads to the formation of stationary anomalies in the vicinity of IL. Honda et al. (2001) focused on the role of Rossby wave propagation in the formation of the northern lobe of the NAO. Our study emphasizes the contribution of transient eddy forcing to the circulation changes along the southern lobe of the NAO.
- Delay in tropical atmospheric response to ENSO
  Kumar and Hoerling (2003) proposed that the lagged atmospheric response to tropical Pacific SST anomalies can be attributed to the seasonality of the total SST field in the tropical eastern Pacific. When SST anomalies associated with El Niño cycle are superimposed on the seasonal cycle of climatological SST,

the total SST reaches a maximum in early spring, 1–3 months later than the peak of SST anomalies. These authors argued that it is the total, rather than anomalous, SST that forces the tropical convective rainfall in the eastern Pacific, which in turn generates the extratropical wave train.

- Influence of extratropical SST anomalies over NA

It has been demonstrated that fluctuations in surface heat fluxes and Ekman transport driven by atmospheric variability are important contributors to extratropical SST variability (e.g., Lau and Nath 2001; Alexander et al. 2002; Alexander and Scott 2002, 2008). The nature of atmospheric response to extratropical SST anomalies is not yet fully understood, largely due to the high-level internal variability of the midlatitude atmosphere, which tends to obscure any direct effect of the underlying SST anomalies. Although the atmospheric response to midlatitude SST forcing is weak, it is not negligible. Hence, extratropical air–sea feedbacks may play a role in the characteristics of the local atmospheric variability, especially during the transition seasons when the atmospheric internal variability is reduced (see review by Kushnir et al. 2002, and references therein). As shown in Fig. 14a, a tripolar pattern of North Atlantic SST anomalies (e.g., Deser and Blackmon 1993; Kushnir 1994) is discernible in the ENSO+/NAO− minus ENSO+/NAO+ composites for the FMA(1) period, with a cold anomaly centered at 30°N being straddled by warm anomalies to the north and south. The air–sea coupling associated with this characteristic SST pattern may exert considerable influences on the prevalent atmospheric circulation patterns over the NA. More study is needed to clarify the processes linking the tripolar SST pattern to NAO variability.

- Stratosphere–troposphere coupling

It has been noted that strong El Niño events are associated with weakening of the stratospheric polar vortex (Labitzke and van Loon 1999; Taguchi and Hartmann 2006), which in turn can affect the late-winter climate in the North Atlantic–European region through downward propagation (e.g., Baldwin and Dunkerton 2001; Sassi et al. 2004; García-Herrera et al. 2006; Manzini et al. 2006). Because of the low vertical resolution of the model stratosphere in CM2.1 (see section 2a), the El Niño effect on the simulated extratropical stratosphere is very weak. The geopotential height anomaly associated with El Niño events at 50 mb (not shown) is about 3–4 times weaker than that of the corresponding signal based on observations and other simulations with an adequate representation of the upper atmosphere (see Fig. 3 in Cagnazzo and Manzini 2009). In the CM2.1 simulation, a weak easterly

anomaly (<-1 m s^{-1}) in the zonal mean zonal wind at 60°N appears almost simultaneously at all pressure levels in March and April (not shown). This pattern is quite different from those in observations and other GCM simulations [see Fig. 4 in Manzini et al. (2006) and Fig. 4 in Ineson and Scaife (2009)], with easterly anomalies (on the order of -10 m s^{-1}) propagating downward from the upper stratosphere in early winter to the lower stratosphere and troposphere in late winter. The feeble stratosphere signals in the CM2.1 experiment might partially explain the reduced north–south SLP gradient across the NA, and also the 2-month delay in the occurrence of the positive anomalies in the northern lobe of the NAO pattern relative to the negative anomalies in the southern lobe (see Fig. 4d).

It would be worthwhile to explore the importance of stratospheric processes in the ENSO–NAO relationship using a GCM with a more realistic upper atmosphere. Recently, a new GFDL climate model (CM3) has been developed, with altogether 48 vertical levels and a model top at 0.01 mb (Donner et al. 2011). The correlation between the ENSO and NAO indices based on output from this model is noticeably stronger than that inferred from the CM2.1 simulation. Diagnosis of the stratosphere–troposphere coupling accompanying ENSO events in this new model is currently under way.

Finally, it should be borne in mind that this study focuses on the seasonally averaged characteristics of the transient eddy forcing associated with the ENSO cycle. The zonally extended pattern of the rms of bandpass-filtered geopotential height (see shading in Fig. 8) from NP to NA is suggestive of strengthened linkages between the Pacific and Atlantic storm tracks during ENSO events. However, such seasonal statistics by themselves do not provide explicit evidence on the propagation of individual eddies from NP to NA. Moreover, the NAO variability is related to the behavior of large-scale persistent and recurrent flow patterns, also known as weather regimes (e.g., Vautard 1990; Cassou et al. 2004, 2005; Straus et al. 2007), with typical time scales on the order of only 10 days (Feldstein 2000). The seasonal results shown in this study represent averages over several episodes of shorter durations. It is, hence, of interest to examine the nature of, and the dynamical processes associated with, these individual episodes in greater detail. In the companion article (Li and Lau 2011, manuscript submitted to *J. Climate*), we shall analyze the daily data in the 2000-yr simulation of CM2.1, so as to illustrate the detailed spatiotemporal evolution of various meteorological phenomena associated with persistent anomalous circulation episodes in the North Pacific–North American–North Atlantic sector. Evidence will be shown on the

downstream development of the wave packet in the course of these persistent episodes. The effects of the subsequent barotropic forcing due to synoptic-scale eddies embedded in the wave packets on the formation of the more slowly-varying flow pattern over NA will also be examined.

APPENDIX

Partial Correlation Coefficient

The partial correlation coefficient $r_{12.3}$ between two variables, A_1 and A_2, with the contribution from A_3 being removed from both, is given by

$$r_{12.3} = \frac{r_{12} - r_{13}r_{23}}{\sqrt{(1 - r_{13}^2)(1 - r_{23}^2)}}, \quad (A1)$$

where the term r_{ij} represents the linear correlation coefficient between A_i and A_j.

REFERENCES

Adler, R. F., and Coauthors, 2003: The version-2 Global Precipitation Climatology Project (GPCP) monthly precipitation analysis (1979–present). *J. Hydrometeor.,* **4,** 1147–1167.

Alexander, M. A., and J. D. Scott, 2002: The influence of ENSO on air–sea interaction in the Atlantic. *Geophys. Res. Lett.,* **29,** 1701, doi:10.1029/2001GL014347.

——, and ——, 2008: The role of Ekman ocean heat transport in the Northern Hemisphere response to ENSO. *J. Climate,* **21,** 5688–5707.

——, I. Bladé, M. Newman, J. R. Lanzante, N.-C. Lau, and J. D. Scott, 2002: The atmospheric bridge: Influence of ENSO teleconnnections on air–sea interaction over the global oceans. *J. Climate,* **15,** 2205–2231.

Annamalai, H., H. Okajima, and M. Watanabe, 2007: Possible impact of the Indian Ocean SST on the Northern Hemisphere circulation during El Niño. *J. Climate,* **20,** 3164–3189.

Baldwin, M. P., and T. J. Dunkerton, 2001: Stratospheric harbingers of anomalous weather regimes. *Science,* **294,** 581–584.

Bell, C. J., L. J. Gray, A. J. Charlton-Perez, M. M. Joshi, and A. A. Scaife, 2009: Stratospheric communication of El Niño teleconnections to European winter. *J. Climate,* **22,** 4083–4096.

Benedict, J. J., S. Lee, and S. B. Feldstein, 2004: Synoptic view of the North Atlantic Oscillation. *J. Atmos. Sci.,* **61,** 121–144.

Bjerknes, J., 1969: Atmospheric teleconnections from the equatorial Pacific. *Mon. Wea. Rev.,* **97,** 163–172.

Branstator, G., 1992: The maintenance of low-frequency atmospheric anomalies. *J. Atmos. Sci.,* **49,** 1924–1946.

——, 1995: Organization of storm track anomalies by recurring low-frequency circulation anomalies. *J. Atmos. Sci.,* **52,** 207–226.

Branston, A., and R. E. Livezey, 1987: Classification, seasonality, and persistence of low-frequency circulation patterns. *Mon. Wea. Rev.,* **115,** 1083–1126.

Brönnimann, S., 2007: Impact of El Niño–Southern Oscillation on European climate. *Rev. Geophys.,* **45,** RG3003, doi:10.1029/2006RG000199.

——, J. Luterbacher, J. Staehelin, T. M. Svendby, G. Hansen, and T. Svenœ, 2004: Extreme climate of the global troposphere and stratosphere 1940–1942 related to El Niño. *Nature,* **431,** 971–974.

——, E. Xoplaki, C. Casty, A. Pauling, and J. Luterbacher, 2007: ENSO influence on Europe during the last centuries. *Climate Dyn.,* **28,** 181–197.

Cagnazzo, C., and E. Manzini, 2009: Impact of the stratosphere on the winter tropospheric teleconnections between ENSO and the North Atlantic and European region. *J. Climate,* **22,** 1223–1238.

Cassou, C., L. Terray, J. W. Hurrell, and C. Deser, 2004: North Atlantic wintertime climate regimes: Spatial asymmetry, stationarity with time, and oceanic forcing. *J. Climate,* **17,** 1055–1068.

——, ——, and A. S. Phillips, 2005: Tropical Atlantic influence on European heat waves. *J. Climate,* **18,** 2805–2811.

Chang, E. K. M., 1998: Poleward-propagating angular momentum perturbations induced by zonally symmetric heat sources in the tropics. *J. Atmos. Sci.,* **55,** 2229–2248.

Compo, G., J. Whitaker, and P. Sardeshmukh, 2006: Feasibility of a 100-year reanalysis using only surface pressure data. *Bull. Amer. Meteor. Soc.,* **87,** 175–190.

Delworth, T. L., and Coauthors, 2006: GFDL's CM2 global coupled climate models. Part I: Formulation and simulation characteristics. *J. Climate,* **19,** 643–674.

Deser, C., and M. L. Blackmon, 1993: Surface climate variations over the North Atlantic Ocean during winter: 1900–93. *J. Climate,* **6,** 1743–1753.

Dong, B.-W., R. T. Sutton, S. P. Jewson, A. O'Neil, and J. M. Slingo, 2000: Predictable winter climate in the North Atlantic sector during the 1997–1999 ENSO cycle. *Geophys. Res. Lett.,* **27,** 985–988.

Donner, L. J., and Coauthors, 2011: The dynamical core, physical parameterizations, and basic simulation characteristics of the atmospheric component AM3 of the GFDL Global Coupled Model CM3. *J. Climate,* **24,** 3484–3519.

Duchon, C., 1979: Lanczos filtering in one and two dimensions. *J. Appl. Meteor.,* **18,** 1016–1022.

Feldstein, S. B., 2000: The timescale, power spectra, and climate noise properties of teleconnection patterns. *J. Climate,* **13,** 4430–4440.

Fraedrich, K., 1994: An ENSO impact on Europe? A review. *Tellus,* **46,** 541–552.

——, and K. Müller, 1992: Climate anomalies in Europe associated with ENSO extremes. *Int. J. Climatol.,* **12,** 25–31.

Franzke, C., S. Lee, and S. B. Feldstein, 2004: Is the North Atlantic Oscillation a breaking wave? *J. Atmos. Sci.,* **61,** 145–160.

García-Herrera, R., N. Calvo, R. R. Garica, and M. A. Giorgetta, 2006: Propagation of ENSO temperature signals into the middle atmosphere. *J. Geophys. Res.,* **111,** D06101, doi:10.1029/2005JD006061.

GFDL Global Atmospheric Model Development Team, 2004: The new GFDL global atmosphere and land model AM2–LM2: Evaluation with prescribed SST simulations. *J. Climate,* **17,** 4641–4673.

Gnanadesikan, A., and Coauthors, 2006: GFDL's CM2 global coupled climate models. Part II: The baseline ocean simulation. *J. Climate,* **19,** 675–697.

Gouirand, I., and V. Moron, 2003: Variability of the impact of El Niño–Southern Oscillation on sea-level pressure anomalies over the North Atlantic in January to March (1874–1996). *Int. J. Climatol.,* **23,** 1549–1566.

——, ——, and E. Zorita, 2007: Teleconnections between ENSO and North Atlantic in an ECHO-G simulation of the 1000–1990 period. *Geophys. Res. Lett.,* **34,** L06705, doi:10.1029/2006GL028852.

Greatbatch, R. J., J. Lu, and K. A. Peterson, 2004: Nonstationary impact of ENSO on Euro-Atlantic winter climate. *Geophys. Res. Lett.,* **31,** L02208, doi:10.1029/2003GL018542.

Griffies, S. M., M. J. Harrison, R. C. Pacanowski, and A. Rosati, 2004: A technical guide to MOM4. GFDL Ocean Group Tech. Rep. 5, NOAA/Geophysical Fluid Dynamics Laboratory, 342 pp.

Hamilton, K., 1988: A detailed examination of the extratropical response to tropical El Niño/Southern Oscillation events. *Int. J. Climatol.,* **8,** 67–86.

Held, I. M., S. W. Lyons, and S. Nigam, 1989: Transients and the extratropical response to El Niño. *J. Atmos. Sci.,* **46,** 163–174.

Hoerling, M. P., and M. Ting, 1994: Organization of extratropical transients during El Niño. *J. Climate,* **7,** 745–766.

——, A. Kumar, and M. Zhong, 1997: El Niño, La Niña, and the nonlinearity of their teleconnections. *J. Climate,* **10,** 1769–1786.

——, J. W. Hurrell, and T. Y. Xu, 2001: Tropical origins for recent North Atlantic climate change. *Science,* **292,** 90–92.

Honda, M., H. Nakamura, J. Ukita, I. Kousaka, and K. Takeuchi, 2001: Interannual seesaw between the Aleutian and Icelandic lows. Part I: Seasonal dependence and life cycle. *J. Climate,* **14,** 1029–1042.

Horel, J. D., and J. M. Wallace, 1981: Planetary-scale atmospheric phenomena associated with the Southern Oscillation. *Mon. Wea. Rev.,* **109,** 813–829.

Hoskins, B. J., and P. J. Valdes, 1990: On the existence of storm-tracks. *J. Atmos. Sci.,* **47,** 1854–1864.

——, I. N. James, and G. H. White, 1983: The shape, propagation and mean-flow interaction of large-scale weather systems. *J. Atmos. Sci.,* **40,** 1595–1612.

Hurrell, J. W., 1995a: Decadal trends in the North Atlantic Oscillation regional temperatures and precipitation. *Science,* **269,** 676–679.

——, 1995b: Transient eddy forcing of the rotational flow during northern winter. *J. Atmos. Sci.,* **52,** 2286–2301.

——, 1996: Influence of variations in extratropical wintertime teleconnections on Northern Hemisphere temperatures. *Geophys. Res. Lett.,* **23,** 665–668.

——, and H. van Loon, 1997: Decadal variations in climate associated with the North Atlantic Oscillation. *Climate Change,* **36,** 301–326.

Ineson, S., and A. A. Scaife, 2009: The role of the stratosphere in the European climate response to El Niño. *Nat. Geosci.,* **2,** 32–36, doi:10.1038/ngeo381.

Kalnay, E., and Coauthors, 1996: The NCEP/NCAR 40-Year Reanalysis Project. *Bull. Amer. Meteor. Soc.,* **77,** 437–471.

Kok, C. J., and J. D. Opsteegh, 1985: Possible causes of anomalies in seasonal mean circulation patterns during the 1982/83 El Niño event. *J. Atmos. Sci.,* **42,** 677–694.

Kumar, A., and M. P. Hoerling, 1997: Interpretation and implications of the observed inter–El Niño variability. *J. Climate,* **10,** 83–91.

——, and ——, 2003: The nature and causes for the delayed atmospheric response to El Niño. *J. Climate,* **16,** 1391–1403.

Kushnir, Y., 1994: Interdecadal variations in North Atlantic sea surface temperature and associated atmospheric conditions. *J. Climate,* **7,** 142–157.

——, W. A. Robinson, I. Bladè, N. M. J. Hall, S. Peng, and R. Sutton, 2002: Atmospheric GCM response to extratropical SST anomalies: Synthesis and evaluation. *J. Climate,* **15,** 2233–2256.

Kwon, Y.-O., M. A. Alexander, N. A. Bond, C. Frankignoul, H. Nakamura, B. Qiu, and L. A. Thompson, 2010: Role of the Gulf Stream and Kuroshio–Oyashio systems in large-scale atmosphere–ocean interaction: A review. *J. Climate,* **23,** 3249–3281.

Labitzke, K. G., and H. van Loon, 1999: *The Stratosphere: Phenomena, History, and Relevance.* Springer-Verlag, 190 pp.

Larkin, N. K., and D. E. Harrison, 2005: Global seasonal temperature and precipitation anomalies during El Niño autumn and winter. *Geophys. Res. Lett.,* **32,** L16705, doi:10.1029/2005GL022860.

Lau, N.-C., 1988: Variability of the observed midlatitude storm tracks in relation to low-frequency changes in the circulation pattern. *J. Atmos. Sci.,* **45,** 2718–2743.

——, and E. O. Holopainen, 1984: Transient eddy forcing of the time-mean flow as identified by quasi-geostrophic tendencies. *J. Atmos. Sci.,* **41,** 313–328.

——, and M. J. Nath, 1991: Variability of the baroclinic and barotropic transient eddy forcing associated with monthly changes in the midlatitude storm tracks. *J. Atmos. Sci.,* **48,** 2589–2631.

——, and ——, 1996: The role of the "atmospheric bridge" in linking tropical Pacific ENSO events to extratropical SST anomalies. *J. Climate,* **9,** 2036–2057.

——, and ——, 2001: Impact of ENSO on SST variability in the North Pacific and North Atlantic: Seasonal dependence and role of extratropical sea–air coupling. *J. Climate,* **14,** 2846–2866.

——, and ——, 2004: Coupled GCM simulation of atmosphere–ocean variability associated with zonally asymmetric SST changes in the tropical Indian Ocean. *J. Climate,* **17,** 245–265.

——, and ——, 2009: A model investigation of the role of air–sea interaction in the climatological evolution and ENSO-related variability of the summer monsoon over the South China Sea and western North Pacific. *J. Climate,* **22,** 4771–4792.

——, A. Leetmaa, M. J. Nath, and H.-L. Wang, 2005: Influences of ENSO-induced Indo–Western Pacific SST anomalies on extratropical atmospheric variability during the boreal summer. *J. Climate,* **18,** 2922–2942.

Lin, S.-J., 2004: A "vertically Lagrangian" finite-volume dynamical core for global models. *Mon. Wea. Rev.,* **132,** 2293–2307.

Manzini, E., M. A. Giorgetta, M. Esch, L. Kornblueh, and E. Roeckner, 2006: The influence of sea surface temperatures on the northern winter stratosphere: Ensemble simulations with the MAECHAM5 model. *J. Climate,* **19,** 3863–3881.

Mathieu, P.-P., R. T. Sutton, B. Dong, and M. Collins, 2004: Predictability of winter climate over the North Atlantic European region during ENSO events. *J. Climate,* **17,** 1953–1974.

Merkel, U., and M. Latif, 2002: A high resolution AGCM study of the El Niño impact on the North Atlantic/European sector. *Geophys. Res. Lett.,* **29,** 1291, doi:10.1020/2001GL013726.

Moron, V., and I. Gouirand, 2003: Seasonal modulation of the El Niño-Southern Oscillation relationship with sea level pressure anomalies over the North Atlantic in October–March (1873–1996). *Int. J. Climatol.,* **37,** 143–155.

Müller, W. A., and E. Roeckner, 2006: ENSO impact on midlatitude circulation patterns in future climate change projections. *Geophys. Res. Lett.,* **33,** L05711, doi:1029/2005GL025032.

Nakamura, H., M. Nakamura, and J. L. Anderson, 1997: The role of high- and low-frequency dynamics in blocking formation. *Mon. Wea. Rev.,* **125,** 2074–2093.

Nigam, S., 2003: Teleconnections. *Encyclopedia of Atmospheric Sciences,* J. R. Holton, J. A. Pyle, and J. A. Curry, Eds., Vol. 6, Academic Press, 2243–2269.

Orlanski, I., 1998: Poleward deflection of storm tracks. *J. Atmos. Sci.,* **55,** 2577–2602.

——, 2005: A new look at the Pacific storm track variability: Sensitivity to tropical SSTs and to upstream seeding. *J. Atmos. Sci.,* **62,** 1367–1390.

Pozo-Vázquez, D., M. J. Esteban-Parra, F. S. Rodrigo, and Y. Castro-Diez, 2001: The association between ENSO and winter atmospheric circulation and temperature in the North Atlantic region. *J. Climate,* **14,** 3408–3420.

——, S. R. Gámiz-Fortis, J. Tovar-Pescador, M. J. Esteban-Parra, and Y. Castro-Dìez, 2005: North Atlantic winter SLP anomalies based on the autumn ENSO state. *J. Climate,* **18,** 97–103.

Rivière, G., and I. Orlanski, 2007: Characteristics of the Atlantic storm-track eddy activity and its relation with the North Atlantic Oscillation. *J. Atmos. Sci.,* **64,** 241–266.

Rogers, J. C., 1984: The association between the North Atlantic Oscillation and the Southern Oscillation in the Northern Hemisphere. *Mon. Wea. Rev.,* **112,** 1999–2015.

Sassi, F., D. Kinnison, B. A. Boville, R. R. Garcia, and R. Roble, 2004: Effect of El Niño–Southern Oscillation on the dynamical, thermal, and chemical structure of the middle atmosphere. *J. Geophys. Res.,* **109,** D17108, doi:10.1029/2003JD004434.

Seager, R., N. Harnik, Y. Kushnir, W. Robinson, and J. Miller, 2003: Mechanisms of hemispherically symmetric climate variability. *J. Climate,* **16,** 2960–2978.

——, Y. Kushnir, J. Nakamura, M. Ting, and N. Naik, 2010: Northern Hemisphere winter snow anomalies: ENSO, NAO and the winter of 2009/10. *Geophys. Res. Lett.,* **37,** L14703, doi:10.1029/2010GL043830.

Smirnov, N. V., 1948: Table for estimating the goodness of fit of empirical distributions. *Ann. Math. Stat.,* **19,** 279–281.

Smith, T. M., R. W. Reynolds, T. C. Peterson, and J. Lawrimore, 2008: Improvements to NOAA's historical merged land–ocean surface temperature analysis (1880–2006). *J. Climate,* **21,** 2283–2296.

Spiegel, M. R., 1988: *Schaum's Outline of Theory and Problems of Statistics*. 2nd ed. McGraw-Hill, 504 pp.

Straus, D. M., S. Corti, and F. Molteni, 2007: Circulation regimes: Chaotic variability versus SST-forced predictability. *J. Climate,* **20,** 2251–2272.

——, and J. Shukla, 1997: Variations of midlatitude transient dynamics associated with ENSO. *J. Atmos. Sci.,* **54,** 777–790.

——, and ——, 2002: Does ENSO force the PNA? *J. Climate,* **15,** 2340–2358.

Taguchi, M., and D. L. Hartmann, 2006: Increased occurrence of stratospheric sudden warmings during El Niño as simulated by WACCM. *J. Climate,* **19,** 324–332.

Thompson, D. W. J., and J. M. Wallace, 2001: Regional climate impacts of the Northern Hemisphere annular mode. *Science,* **293,** 85–89.

Toniazzo, T., and A. A. Scaife, 2006: The influence of ENSO on winter North Atlantic climate. *Geophys. Res. Lett.,* **33,** L24704, doi:10.1029/2006GL027881.

Trenberth, K. E., 1986: An assessment of the impact of transient eddies on the zonal flow during a blocking episode using localized Eliassen–Palm flux diagnostics. *J. Atmos. Sci.,* **43,** 2070–2087.

——, G. W. Branstator, D. Karoly, A. Kumar, N.-C. Lau, and C. Ropelewski, 1998: Progress during TOGA in understanding and modeling global teleconnections associated with tropical sea surface temperatures. *J. Geophys. Res.,* **103,** 14 291–14 324.

van Loon, H., and J. C. Rogers, 1978: The seesaw in winter temperatures between Greenland and northern Europe. *Mon. Wea. Rev.,* **106,** 296–310.

Vautard, R., 1990: Multiple weather regimes over the North Atlantic: Analysis of precursors and successors. *Mon. Wea. Rev.,* **118,** 2057–2081.

Walker, G. T., and E. W. Bliss, 1932: World weather V. *Mem. Roy. Meteor. Soc.,* **4,** 53–84.

Wallace, J. M., and D. S. Gutzler, 1981: Teleconnections in the geopotential height field during the Northern Hemisphere winter. *Mon. Wea. Rev.,* **109,** 784–812.

Whitaker, J. S., G. P. Compo, X. Wei, and T. M. Hamill, 2004: Reanalysis without radiosondes using ensemble data assimilation. *Mon. Wea. Rev.,* **132,** 1190–1200.

Wittenberg, A. T., 2009: Are historical records sufficient to constrain ENSO simulations? *Geophys. Res. Lett.,* **36,** L12702, doi:10.1029/2009GL038710.

——, A. Rosati, N.-C. Lau, and J. J. Ploshay, 2006: GFDL's CM2 global coupled climate models. Part III: Tropical Pacific climate and ENSO. *J. Climate,* **19,** 698–722.

Xue, Y., T. M. Smith, and R. W. Reynolds, 2003: Interdecadal changes of 30-yr SST normals during 1871–2000. *J. Climate,* **16,** 1601–1612.

Zhang, Y., and I. M. Held, 1999: A linear stochastic model of a GCM's midlatitude storm tracks. *J. Atmos. Sci.,* **56,** 3416–3435.